

Diploma thesis
For obtaining the academic degree Mag.rer.nat.

Simulation of optical properties of surface plasmons in silver nanodiscs

MICHAEL REISECKER
Graz, April 2014

Supervisor: Ao. Univ. Prof. Dr. ULRICH HOHENESTER



Karl-Franzens-Universität Graz
Institute of Physics
Department of Theoretical Physics

To people following their dreams,
including my parents.

Abstract

Silver nanodiscs embedded in a dielectric environment can be used to confine light to their surface, squeezing the electromagnetic fields to form standing waves on the nanoscale. These standing waves can have different wavelengths and define the resonant modes of the disc. Many such modes exist, but not all of them can couple to a light wave as they need to have a dipole moment, matching the symmetric nature of an electromagnetic wave. These modes are called *bright plasmonic modes*.

Dark plasmonic modes with no dipole moment have been studied with electron energy loss spectroscopy, and in the last years a new type of mode family came to the attention of researchers. Distinct from the well-known *edge modes* with azimuthal symmetry and nodes around the edge of the disc, these dark *film modes* are radially symmetric and were termed “breathing modes”. However, for large enough discs in the range of a couple of hundred nanometers retardation effects come into play and can be effectively used to break the symmetry of the system and excite dark modes optically. The coupling of the first order breathing mode (among others) is demonstrated in this thesis using computer simulations.

The symmetry restrictions of a dipole-like excitation can also be relaxed by placing an oscillating dipole close enough to a nanodisc so that its field strongly varies locally. Consequently, such emitters can also couple resonantly to dark modes resulting in a faster decay of the emitter. This mechanism allows for radiationless energy transfer between a donor molecule and an acceptor molecule. Our simulations show that the donor can couple to the nanodisc which transfers energy mainly to its nodes where it can be picked up by the acceptor.

Contents

1 Prologue	1
1.1 Introduction	1
1.2 Structure of this thesis	3
2 Theoretical principles	5
2.1 Electrostatic basics	5
2.2 Maxwell's theory of electromagnetism	6
2.2.1 Maxwell's equations	7
2.2.2 Quasistatic approximation	8
2.2.3 Green's function in the quasistatic regime	8
2.2.4 Boundary conditions and the interface between two different media	9
2.2.5 Boundary element method	10
2.2.6 Retarded solution	11
2.2.7 Dielectric function of metals	12
2.3 Nano optics	15
2.3.1 Classical versus quantum approach	15
2.3.2 Lifetime and decay rates of an emitter	15
2.3.3 Quantum yield	16
2.3.4 Cross sections	17
2.3.5 Energy transfer between quantum emitters	20
2.4 Plasmons	22
2.4.1 Surface plasmons	23
2.4.2 Particle plasmons	24
2.4.3 Bulk plasmons	26
2.4.4 Excitation of plasmons	26
2.5 Plasmons confined to nanoparticles	27
2.5.1 Surface and edge modes	27
2.5.2 Breathing modes	28
2.5.3 Bright and dark plasmonic modes	29
3 Plasmon simulation	31
3.1 Imaging of plasmons	31
3.1.1 Plane wave excitation	31
3.1.2 Dipole excitation	31
3.1.3 Electron energy loss spectroscopy	35

Contents

3.2	Simulating nanodiscs	36
3.2.1	The MNPBEM toolbox	36
3.2.2	Structure and discretization	37
3.2.3	BEM simulations	38
4	Results	39
4.1	EELS excitation	39
4.1.1	The mode spectrum of a nanodisc	39
4.1.2	Surface charges	40
4.2	Plane wave excitation	44
4.2.1	Straight impact	44
4.2.2	Tilted impact	45
4.2.3	Dependence on disc size	46
4.2.4	Polarization dependence	47
4.2.5	Dependence on the index of the surrounding medium	48
4.2.6	Comparison between silver and gold	49
4.2.7	Experimental results	50
4.3	Dipole excitation	50
4.3.1	Coupling of dipoles to dark modes	51
4.3.2	Dependence on the dipoles' orientation	54
4.3.3	Quantum yield	54
4.4	Förster type energy transfer	57
4.4.1	Energy transfer in free space	57
4.4.2	Energy transfer in presence of nanodisc	58
5	Summary and outlook	65
5.1	Summary	65
5.2	Outlook	65
6	Acknowledgements	67
	Bibliography	69
	List of Figures	73

1 Prologue

1.1 Introduction

Plasmonics is a recently blossoming field of research that engages in understanding phenomena occurring at the bridge between classical physics and quantum mechanics, especially regarding electromagnetic properties of tiny metallic particles. Those particles are several to several hundreds of nanometers small, and therefore close the gap between the microscopic and the macroscopic world.

The optical features of *metallic nanoparticles* and their interesting response to illuminating light have long been exploited. A famous example – the *Lycurgus cup* – dates back to the 4th century where golden nanoparticles were dispersed in glass, although most likely not in a controlled manner and maybe not even knowingly. The cup appears green if lighted from the front and red if lighted from the back (Fig. 1.1). Another everyday example are the colors of church windows. They too are accomplished with metallic nanoparticles in the glass which makes them durable and somewhat special, if not beautiful.



Fig. 1.1: The antique Lycurgus cup showing different behavior for reflected and absorbed light.

Courtesy of the British Museum, London

The framework for a classical approach to mathematically describe metallic nanoparticles is not new either. Maxwell's equations from the 19th century sum up the knowl-

1 Prologue

edge needed to understand phenomena occurring at the interface of a metal and a dielectric and they are still applicable on the moderate nano scale. They constitute the underlying theory to investigate *surface plasmons* which are the quasiparticles of free electron gas density oscillations in a metal. The plasmons' different resonant behavior for scattered and absorbed light is the reason for the Lycurgus cup's different colors depending on the direction of illumination.

However, the term “Plasmonics” as a distinct research topic emerged with more or less recent developments in experimental technology and accompanied computer strength. One of the motivations for the advances in fabrication methods for nanoparticles is to overcome the Abbe diffraction limit of light. Using plasmons, light can be confined to the nanoscale giving rise to optical near-field microscopy. Other thinkable nanotechnological uses include a speed bump in computer chips [Atw07], sensing applications [AHL⁺08], data storage [ZCG09], cancer treatment [ESHES05] and generally matching the industry’s need for miniaturized circuits.

This work focusses purely on theoretically understanding and simulating some of the properties of metallic nanoparticles. As opposed to more common pigments their response to an external excitation (e.g. a light wave) depends strongly on their geometry. It influences the way in which the free electron gas density can oscillate at the surface of the particle resulting in different behaviors for different geometries. Additionally, within a fixed shape more than one resonant oscillation can occur analogous to higher harmonics in mechanical vibrations. Here the particle of choice is the nanodisc because of its symmetric nature while still being able to control the very important aspect ratio. Common choices for the material are gold and silver because of their relatively small Ohmic losses.

Some of the resonant plasma oscillations (modes) have been studied in detail, the most intuitive one being the dipole mode with an accumulated negative charge on one side of the particle and a positive one on the other side. But apart from these multipole modes with distinct poles (regions of the same surface charge) along the edge of the disc there exists a different type of mode family – the so-called breathing modes. The associated surface charge oscillations strive outwards, and areas of the same charge form rings around the center of the disc. Principally light can only couple to the dipole mode or other modes with a dipole moment. The breathing mode possesses no dipole moment and remained optically hidden thus far. However, by using oblique light retardation effects can be used in a way that the electric field’s symmetry is broken and this restriction is rendered void. This is the central aspect of this work.

Using computer simulations the optical mode spectrum of a silver nanodisc is investigated. The results show that the breathing mode indeed lights up when tilting the light source. These measurements are backed by electron energy loss spectroscopy (EELS) simulations where the excitation is an electron beam which can couple to both dark and bright modes. In fact, the breathing mode was discovered using this technique [SDH⁺12]. A third type of excitation is also used, namely the excitation with an oscillating dipole in the nanodisc’s vicinity. The dipole represents a molecule situated close to the metallic nanoparticle. This setup composes an interesting system

in which the molecule can interact with the metal. It is shown that the nanodisc can strongly enhance the dipole's decay rate, effectively being used as an antenna. A systematic overview is presented for varying disc sizes, refractive indices of the surrounding medium, the orientation of the dipoles and the relation between energy that is transported to the far field and energy that flows into other channels. Related to this effect is the energy transfer between a donor and an acceptor molecule in connection with a nanodisc, which is also a topic of this work. The nanodisc, if tuned appropriately, can enhance the transfer rate, mostly at the poles of the modes the dipole couples to.

1.2 Structure of this thesis

Subsequent to this introduction the thesis is quite strictly split up into theory and results. This is meant to allow readers familiar with the subject to skip the textbook knowledge which is presented in the second chapter.

We will start with summing up Maxwell's theory of electromagnetism and how it can be made accessible for computer simulations via discrete surface elements. After describing the Drude model for metals we turn to some of the observables that will actually be calculated like the decay rate of an emitter, the ratio between radiative and non-radiative decay rate (quantum yield), cross sections and energy transfer between two dipoles. Afterwards, the concept of plasmons is developed, and we investigate how they can be excited. This covers the different types of plasmons, the system that is needed to excite the plasmons, and the different kinds of excitations (modes) that can occur once this has been accomplished. We conclude the theoretical part by describing three specific kinds of excitation in the third chapter – a plane wave, an oscillating emitter and an electron beam.

The fourth chapter is devoted to displaying the results obtained in the computer simulations. We give an overview of the modes of a silver nanodisc excited via electron energy loss spectroscopy. We then turn to the excitation with an incident light beam and vary the parameters of the system like the refractive index, the disc size and, most importantly, the angle of the incoming light. The next section deals with dipole excitation, and the positions and energies of dipoles that are placed close to a nanodisc are varied to be able to couple to the disc and exhibit an enhanced decay rate. In the last section energy transfer between a donor molecule and an acceptor molecule is simulated.

The thesis is closed with a summary, an outlook of what's left to do, acknowledgements, a bibliography of the cited works and a list of figures.

2 Theoretical principles

2.1 Electrostatic basics

Let us quickly remind ourselves of some elementary terms needed in the following chapters.

Electrostatics examines phenomena that occur in presence of resting (static) electric charges. Experimentally, the force between two charges Q and q was determined in Coulomb's law to be

$$\mathbf{F}(\mathbf{r}) = f \frac{Qq}{r^2} \hat{\mathbf{r}}.$$

Measuring \mathbf{F} in Newton and r in meters, the dimensions of the proportionality factor f and the charge Q could be chosen. This evolved into two systems of units, the *SI*-system and the *cgs*-system. In the SI-system, Q was chosen as the charge transported by a constant current of one ampere in one second, thus $[Q] = A \cdot s$. An experiment determined the value of f , which is now written as $f = 1/4\pi\varepsilon_0$. The cgs-system, often used in theoretical works, sets f to 1. Dividing \mathbf{F} by the test charge q results in the electric field strength

$$\mathbf{E}(\mathbf{r}) = \frac{Q}{4\pi\varepsilon_0 r^2} \hat{\mathbf{r}}.$$

For an expanded charge with continuous charge density $\rho(\mathbf{r})$ the force outside of the volume V of the charged particle is given by:

$$\mathbf{F}(\mathbf{R}) = \frac{q}{4\pi\varepsilon_0} \int_V \frac{\mathbf{R} - \mathbf{r}}{|\mathbf{R} - \mathbf{r}|^3} \rho(\mathbf{r}) dV.$$

The electric flux $d\Phi_{el} = \mathbf{E} \cdot d\mathbf{A}$ is measuring the electric field lines (Fig. 2.1) that penetrate a small area $d\mathbf{A}$. For a closed surface A , Gauss' theorem tells us that

$$\Phi_{el} = \int_A \mathbf{E} \cdot d\mathbf{A} = \int_{V(A)} \text{div } \mathbf{E} dV.$$

A point charge in the middle of a sphere results in the Coulomb field $\mathbf{E} = Q/(4\pi\varepsilon_0 r^2) \hat{\mathbf{r}}$ that yields $\Phi_{el} = Q/\varepsilon_0$ and suggests $\Phi_{el} = \frac{1}{\varepsilon_0} \int \rho dV$, which leads to

$$\text{div } \mathbf{E} = \rho/\varepsilon_0.$$

The electric field is conservative which allows us to assert a unique function $\Phi(P)$, called the electrostatic potential at a point P :

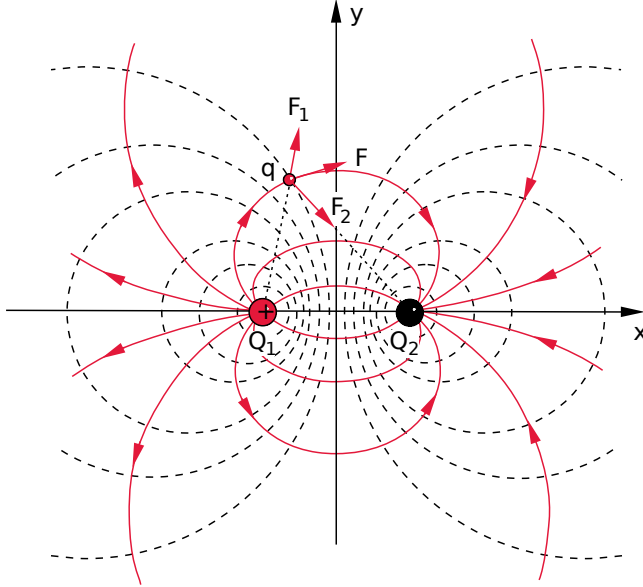


Fig. 2.1: Electric field lines (red) and equipotential lines (dashed) for two opposite charges $Q_1 = -Q_2$ (electric dipole).

Taken from: [Dem06]

$$\Phi(P) = \int_P^\infty \mathbf{E} \cdot d\mathbf{s},$$

or in the other direction

$$\mathbf{E} = -\nabla\Phi.$$

The Poisson equation $\Delta\Phi = -\rho/\epsilon_0$ follows. If the charge distribution is known, the potential and field strength can be calculated.

The product $q \cdot \Phi$ is the work needed to bring a charge q from the point P to infinity. The difference of the potential between two points is the voltage with dimension volts¹.

2.2 Maxwell's theory of electromagnetism

In the 1860s JAMES CLERK MAXWELL² produced a set of partial differential equations of first order that treat electromagnetic fields in vacuum and in macroscopic media, i.e. the relation between electrical and magnetic phenomena [Max65].

¹It is often convenient to define a small energy unit, the electron volt, as the energy an electron gains by experiencing a potential difference of 1V.

²*13.06.1831, Edinburgh, Scotland; †05.11.1879

2.2.1 Maxwell's equations

The four Maxwell equations for a macroscopic medium in differential form read in Gaussian units³:

$$\nabla \cdot \mathbf{D}(\mathbf{r}, t) = 4\pi\rho(\mathbf{r}, t), \quad (2.1a)$$

$$\nabla \cdot \mathbf{B}(\mathbf{r}, t) = 0, \quad (2.1b)$$

$$\nabla \times \mathbf{H}(\mathbf{r}, t) = \frac{4\pi}{c}\mathbf{j} + \frac{1}{c}\frac{\partial \mathbf{D}(\mathbf{r}, t)}{\partial t}, \quad (2.1c)$$

$$\nabla \times \mathbf{E}(\mathbf{r}, t) = -\frac{1}{c}\frac{\partial \mathbf{B}(\mathbf{r}, t)}{\partial t}. \quad (2.1d)$$

Here, \mathbf{D} is the dielectric displacement, \mathbf{B} is the magnetic induction, \mathbf{H} is the magnetic and \mathbf{E} the electric field. \mathbf{j} is the current density and ρ the free charge density. c denotes the speed of light. In the following we assume an isotropic and linear medium $\mathbf{B} = \mu\mathbf{H}$ and $\mathbf{D} = \epsilon\mathbf{E}$ with ϵ being the permittivity and μ the magnetic permeability. ϵ will be assumed constant throughout and at optical frequencies $\mu = 1 + 4\pi\chi_m \approx 1$, meaning that the magnetic component of light is often neglectable. χ_m is the magnetic susceptibility.

Assuming a time dependence of the form $\mathbf{E}(\mathbf{r}, t) = \mathbf{E}(\mathbf{r})e^{-i\omega t}$ with $k = \omega/c$ and taking the curl on Ampère's law (2.1c) and Faraday's law (2.1d) in a source free space in frequency form leads to the wave equation in Helmholtz form:

$$(\nabla^2 + \epsilon k^2)\mathbf{E}(\mathbf{r}, \omega) = 0, \quad (2.2a)$$

$$(\nabla^2 + \epsilon k^2)\mathbf{B}(\mathbf{r}, \omega) = 0. \quad (2.2b)$$

This equation postulates electromagnetic waves.

Introducing the vector potential \mathbf{A} and the scalar potential Φ we can substitute the following into Maxwell's equations:

$$\mathbf{E} = -\nabla\Phi - \frac{1}{c}\frac{\partial}{\partial t}\mathbf{A}, \quad (2.3a)$$

$$\mathbf{B} = \nabla \times \mathbf{A}. \quad (2.3b)$$

The electric field is not independent of the magnetic field. Using the gauge invariance of the potentials we can choose them such that they fulfill the Lorentz condition [Lor67]

$$\nabla \cdot \mathbf{A} + \epsilon \frac{1}{c} \frac{\partial}{\partial t} \Phi = 0. \quad (2.4)$$

³Gaussian units: $e = m = \hbar = 1$

2 Theoretical principles

This leads to decoupled wave equations for \mathbf{A} and Φ in the following form. They are equivalent to Maxwell's equations and are called the *Helmholtz equations for potentials*:

$$\nabla^2\Phi + k^2\varepsilon\Phi = -4\pi\rho, \quad (2.5a)$$

$$\nabla^2\mathbf{A} + k^2\varepsilon\mathbf{A} = -\frac{4\pi}{c}\mathbf{j}. \quad (2.5b)$$

2.2.2 Quasistatic approximation

A simplified solution to the Helmholtz equations (2.5) can be found by assuming a particle size that is small compared to the wavelength λ , meaning that the incoming electric field is more or less constant in the region of the particle. Thus, $k \approx 0$ and (2.5a) simplifies to the *Poisson equation* (2.6), and if no external charges are present to the *Laplace equation* (2.7) respectively.

$$\nabla^2\Phi = -4\pi\rho \quad (2.6)$$

$$\nabla^2\Phi = 0 \quad (2.7)$$

2.2.3 Green's function in the quasistatic regime

To tackle inhomogeneous differential equations like the Poisson equation, we can use a formalism developed by GEORGE GREEN⁴ [Gre28] and introduce Green's function as

$$\nabla^2G(\mathbf{r}, \mathbf{r}') = -4\pi\delta(\mathbf{r} - \mathbf{r}'), \quad (2.8)$$

with

$$G(\mathbf{r}, \mathbf{r}') = \frac{1}{|\mathbf{r} - \mathbf{r}'|} + F(\mathbf{r}, \mathbf{r}'). \quad (2.9)$$

$F(\mathbf{r}, \mathbf{r}')$ is an arbitrary function fulfilling the Laplace equation $\nabla^2F(\mathbf{r}, \mathbf{r}') = 0$.

With this, the solution to the Poisson equation (2.6) becomes [Jac98, p. 38f.]:

$$\Phi(\mathbf{r}) = \int d\mathbf{r}' G(\mathbf{r}, \mathbf{r}', \varepsilon)\rho(\mathbf{r}'). \quad (2.10)$$

⁴*14.07.1793, Sneinton, England; †31.05.1841

2.2.4 Boundary conditions and the interface between two different media

For homogeneous media with constant $\varepsilon_1, \varepsilon_2$ the volume integral (2.10) can be recast into a surface integral using Gauss' theorem. The solution then becomes [HK05]:

$$\Phi(\mathbf{r}) = \Phi_{\text{ext}}(\mathbf{r}) + \int_{\partial\Omega} ds' G(\mathbf{r}, \mathbf{s}') \sigma(\mathbf{s}'), \quad \mathbf{r} \in \Omega, \quad (2.11)$$

where σ is the surface charge at the interface $\partial\Omega$ between the two media and Φ_{ext} a solution of the free Helmholtz equation. This means that a surface charge σ is introduced which has to be chosen such that the boundary conditions are fulfilled.

Two of the constraints for electromagnetic fields at the border of two media are that the tangential component of the electric field as well as the normal component of the dielectric displacement have to be continuous. $\mathbf{E}_{\varepsilon_1}^{\perp} \propto \mathbf{E}_{\varepsilon_2}^{\perp}$ implies that the scalar potential is continuous which is always fulfilled if $\sigma_1 = \sigma_2$. To be in accordance with $\mathbf{D}_{\varepsilon_1}^{\perp} \propto \mathbf{D}_{\varepsilon_2}^{\perp}$ meaning

$$\hat{\mathbf{n}} \cdot (\varepsilon_1 \nabla \Phi_1 - \varepsilon_2 \nabla \Phi_2) = 0 \quad (2.12)$$

we need to carry out the surface derivative $\hat{\mathbf{n}} \nabla \Phi$ for the potential (2.11) with $\hat{\mathbf{n}}$ being a normal vector to the surface:

$$\lim_{\mathbf{r} \rightarrow \mathbf{s}} \hat{\mathbf{n}} \cdot \nabla \Phi(\mathbf{r}) = \lim_{\mathbf{r} \rightarrow \mathbf{s}} \left[\hat{\mathbf{n}} \cdot \nabla \int_{\partial\Omega} ds' G(\mathbf{r} - \mathbf{s}') \sigma(\mathbf{s}') + \hat{\mathbf{n}} \cdot \nabla \Phi_{\text{ext}} \right]. \quad (2.13)$$

The point of concern is the singularity in G , and the limit $\mathbf{r} \rightarrow \mathbf{s}$ needs further consideration. Let ρ and φ be polar coordinates expressing $\hat{\mathbf{n}}$ as $\hat{\mathbf{e}}_z$, \mathbf{r} as $(0, 0, z)^T$ and \mathbf{s}' as $(\rho \cos \varphi, \rho \sin \varphi, 0)^T$. We now calculate the boundary integral in a circle sufficiently small for σ to be approximately constant [HT08]. Then, the integral

$$\lim_{\mathbf{r} \rightarrow \mathbf{s}} \hat{\mathbf{n}} \cdot \nabla \int_{\partial\Omega} ds' G(\mathbf{r}, \mathbf{s}') \sigma(\mathbf{s}') \quad (2.14)$$

becomes

$$\lim_{z \rightarrow \pm 0} 2\pi z \int_0^R d\rho (\rho^2 + z^2)^{-3/2} = \pm 2\pi, \quad (2.15)$$

with the sign being dependent on the direction the surface is approached from. Using this result we arrive at:

$$\lim_{\mathbf{r} \rightarrow \mathbf{s}} \hat{\mathbf{n}} \cdot \nabla \Phi(\mathbf{r}) = \lim_{\mathbf{r} \rightarrow \mathbf{s}} \left[\hat{\mathbf{n}} \cdot \nabla \int_{\partial\Omega} ds' G(\mathbf{r} - \mathbf{s}') \sigma(\mathbf{s}') \pm 2\pi \sigma(\mathbf{s}) + \hat{\mathbf{n}} \cdot \nabla \Phi_{\text{ext}} \right]. \quad (2.16)$$

2.2.5 Boundary element method

GUSTAV MIE⁵ has solved equation (2.16) for a spherical geometry [Mie08] but the solution for arbitrary geometries remains numerical. Nevertheless, the Mie theory provides a handy check for numerical approaches. As usual, for the numerical computation we need to discretize the borders. The idea of the *boundary element method* (BEM) – the central approach in this work – is to discretize the surface of a region of interest (i.e. a particle) and approximate the small surface elements $\partial\Omega_i$ by discrete points at their center connected by Green's function (Fig. 2.2). Obviously, these computations are less time consuming than methods which rely on discretizing the whole volume.

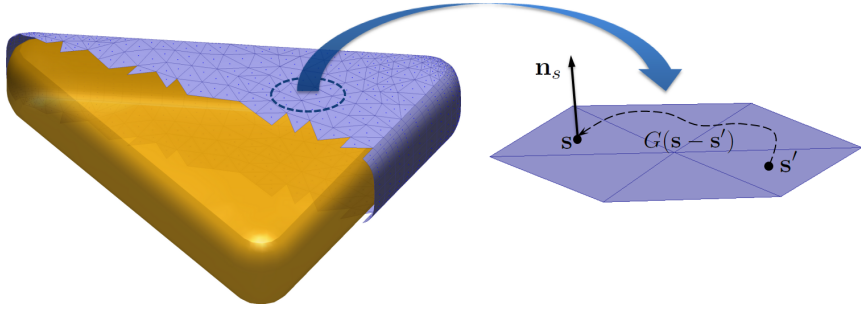


Fig. 2.2: Sketch of the BEM, where a particle is described by its surface which is discretized to surface elements connected by Green's function. Each element has one value for the surface charge sitting at its center.

Taken from: [Trü11]

Let us first introduce the shorthand notation $F(\mathbf{s}, \mathbf{s}') := \hat{\mathbf{n}} \cdot \nabla G(\mathbf{r} - \mathbf{s}')$ and $\lim_{\mathbf{r} \rightarrow \mathbf{s}} \hat{\mathbf{n}} \cdot \nabla \equiv \frac{\partial}{\partial n}$. Then, the integral (2.16) reads

$$\frac{\partial \Phi}{\partial n} = \int_{\partial\Omega} d\mathbf{s}' F(\mathbf{s}, \mathbf{s}') \sigma(\mathbf{s}') \pm 2\pi\sigma(\mathbf{s}) + \frac{\partial \Phi_{\text{ext}}}{\partial n} \quad (2.17)$$

and discretizes to:

$$\left(\frac{\partial \Phi}{\partial n} \right)_i = \sum_j F_{ij} \sigma_j \pm 2\pi\sigma_i + \left(\frac{\partial \Phi_{\text{ext}}}{\partial n} \right)_i, \quad (2.18)$$

or in matrix notation with $\mathbf{F} = F(\mathbf{s}_i, \mathbf{s}_j)$:

$$\frac{\partial \Phi}{\partial n} = \mathbf{F} \boldsymbol{\sigma} \pm 2\pi\boldsymbol{\sigma} + \frac{\partial \Phi_{\text{ext}}}{\partial n}. \quad (2.19)$$

For N surface elements Φ and $\boldsymbol{\sigma}$ are of dimension N , and \mathbf{F} is a $N \times N$ -matrix. From the boundary condition (2.12) it follows that

⁵*29.09.1868, Rostock, Germany; †13.02.1957

$$2\pi\boldsymbol{\sigma}(\varepsilon_1 + \varepsilon_2) + \mathbf{F}\boldsymbol{\sigma}(\varepsilon_1 + \varepsilon_2) = (\varepsilon_1 - \varepsilon_2) \frac{\partial \Phi_{\text{ext}}}{\partial n} \quad (2.20)$$

and from here the final result for the quasistatic surface charge with $\Lambda = 2\pi \frac{\varepsilon_1 + \varepsilon_2}{\varepsilon_2 - \varepsilon_1}$:

$$\boldsymbol{\sigma} = -(\Lambda + \mathbf{F})^{-1} \frac{\partial \Phi_{\text{ext}}}{\partial n}. \quad (2.21)$$

This equation where material parameters are found in $\Lambda(\varepsilon_1, \varepsilon_2)$ and the geometry is incorporated in \mathbf{F} allows us to compute the surface charges $\boldsymbol{\sigma}$ at each discrete point of our surface.

2.2.6 Retarded solution

With increasing particle size we can no longer neglect the spatially dependent electric field and have to consider a wavenumber $k \neq 0$, and solve the full Helmholtz equations with a non-vanishing vector potential \mathbf{A} as given in (2.5). Once again we select the Lorentz gauge (2.4). The Green function now needs to be a solution of

$$(\nabla^2 + k_j^2)G_j(\mathbf{r}, \mathbf{s}') = -4\pi\sigma(\mathbf{r} - \mathbf{s}'), \quad (2.22)$$

which is given by:

$$G_j = \frac{e^{ik_j|\mathbf{r}-\mathbf{s}'|}}{|\mathbf{r} - \mathbf{s}'|} \quad (2.23)$$

with j indexing the medium.

With an appropriate G the full Helmholtz equations can be solved for Φ and \mathbf{A} [dA02]:

$$\Phi(\mathbf{r}) = \int_{\partial\Omega_j} ds' G_j(\mathbf{r}, \mathbf{s}') \sigma_j(\mathbf{s}') + \Phi_{\text{ext}}(\mathbf{r}), \quad (2.24a)$$

$$\mathbf{A}(\mathbf{r}) = \int_{\partial\Omega_j} ds' G_j(\mathbf{r}, \mathbf{s}') \mathbf{h}_j(\mathbf{s}') + \mathbf{A}_{\text{ext}}(\mathbf{r}), \quad (2.24b)$$

with \mathbf{h}_j being the surface currents for different media (while j denotes external currents).

As opposed to the quasistatic case we can no longer construct identical surface charges and currents on different sides of a border. Instead, external potentials must be chosen such that they are only induced by a source (e.g. a plane wave or a dipole) situated directly next to the particle boundary. This means that a source cannot excite a particle that is shielded by some outer surface.

Using the boundary conditions (i.e. the continuity of the potential) after some algebra this leads to the fully retarded surface charges σ_1 and σ_2 and currents \mathbf{h}_1 and \mathbf{h}_2 (see [dA02]).

2.2.7 Dielectric function of metals

To describe how materials interact with an electromagnetic wave, particularly the movement of electrons, a simple but nonetheless for some regions quite accurate model is the *Lorentz-Drude model*. The frequency of the incident wave highly affects the material's behavior which in this model is understood as a harmonic oscillator where the electrons are driven by the external field. To describe metals with a free electron gas where the electrons do not strive back to their original position in a kinetic movement we can set the restoring force to zero and only keep inertia and damping terms to set up the equation of motion for the free electron gas within the *Drude-Sommerfeld theory* to be (consult [NH06, p. 380], or [Dem06, p. 227ff.] for a more basic discussion):

$$m_e \frac{\partial^2 \mathbf{r}}{\partial t^2} + m_e \Gamma \frac{\partial \mathbf{r}}{\partial t} = e \mathbf{E}_0 e^{-\omega t} \quad (2.25)$$

with e and m_e being charge and effective mass of the free electrons and \mathbf{E}_0 and ω are the amplitude and frequency of the applied field. The damping term Γ is directly proportional to the Fermi velocity⁶ and indirectly proportional to the electron mean free path.

The macroscopic polarization \mathbf{P} can be expressed as:

$$\mathbf{P}(\omega) = \epsilon_0 \chi_e(\omega) \mathbf{E}(\omega). \quad (2.26)$$

Comparing this to the frequency-dependent microscopic displacement as given by the oscillator model yields the frequency-dependent dielectric function of the metal:

$$\varepsilon(\omega) = 1 + \chi_e(\omega). \quad (2.27)$$

χ_e can be calculated by solving the equation of motion (2.25) with the ansatz $\mathbf{r}(t) = \mathbf{r}_0 e^{-\omega t}$:

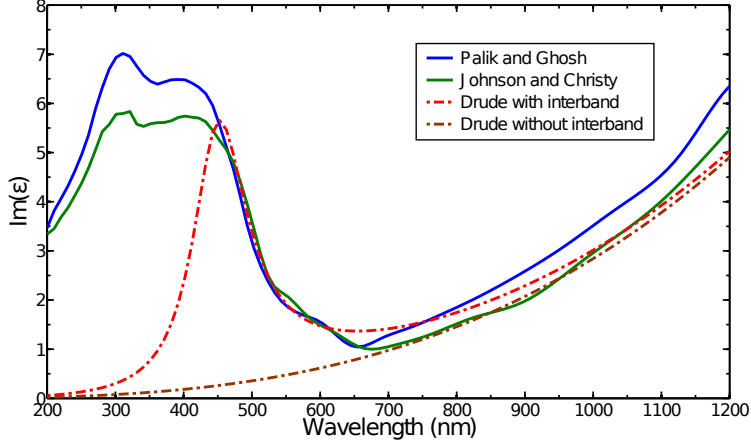
$$\varepsilon_{\text{Drude}} = 1 - \frac{\omega_p^2}{\omega^2 + i\Gamma\omega}, \quad (2.28)$$

where we have used the definition for the plasma frequency $\omega_p = \sqrt{n e^2 / (m_e \epsilon_0)}$.

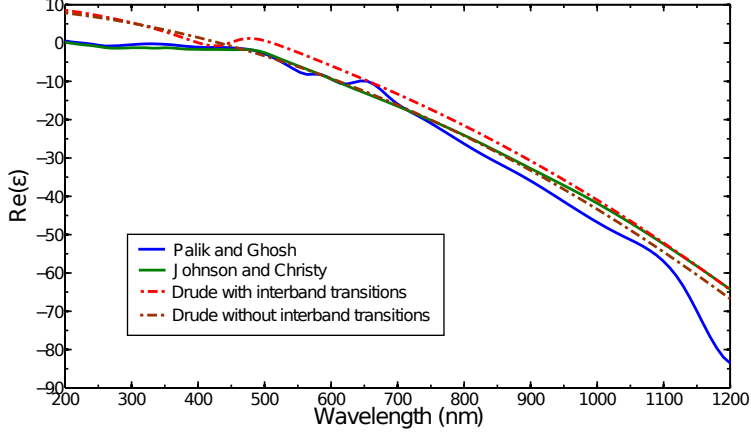
As can be seen in Fig. 2.3a, the Drude-Sommerfeld theory for gold is in good agreement with experimental values for wavelengths greater than ≈ 700 nm. Photons with higher energies, however, can promote lower-lying electrons into the conduction band giving rise to *interband transitions*. These electrons can classically be understood as bound electrons of the metal, and their equation of motion takes this into account by keeping the spring constant α of the potential that binds the electrons:

$$m \frac{\partial^2 \mathbf{r}}{\partial t^2} + m\gamma \frac{\partial \mathbf{r}}{\partial t} + \alpha \mathbf{r} = e \mathbf{E}_0 e^{-\omega t}, \quad (2.29)$$

⁶The Fermi energy is the highest energy in an electron gas at $T = 0$ for which all lower energy levels are filled and all higher levels are empty. The Fermi velocity is the velocity of electrons with the Fermi energy as kinetic energy.



(a) Imaginary part of the dielectric function of gold.



(b) Real part of the dielectric function of gold.

Fig. 2.3: The dielectric function of gold is plotted. Comparison between two experimental datasets [Pal85] and [JC72] (solid lines), the Drude model and the Drude model considering interband transitions (dash-dotted lines). Good agreement for the latter starts at about 450nm.

where m is the effective mass of the bound electrons and γ the damping constant (mainly radiative damping). This leads to the contribution of bound electrons to the dielectric function:

$$\varepsilon_{\text{Interband}}(\omega) = 1 + \frac{\tilde{\omega}_p^2}{\omega_0^2 - \omega^2 - i\gamma\omega}. \quad (2.30)$$

Here, $\tilde{\omega}_p = \sqrt{\tilde{n}e^2/m\varepsilon_0}$ with \tilde{n} the density of the bound electrons and $\omega_0 = \sqrt{\alpha/m}$.

As only one interband transition is taken into account the model is still inefficient

2 Theoretical principles

for wavelengths below ≈ 470 nm; band transitions for higher energies are only treated with a constant offset. We will exclusively use interpolated experimental data in this work.

To give a physical interpretation of the plasma frequency we neglect the damping term (i.e. $\omega \gg \gamma$) in equation (2.28) and simplify it to:

$$\varepsilon_{\text{Drude}} = 1 - \frac{\omega_p^2}{\omega^2}. \quad (2.31)$$

Now two frequency regions can be considered. For $\omega > \omega_p$ the permittivity becomes positive which means that the refractive index is real. For $\omega < \omega_p$ on the other hand, ε and therefore the refractive index become imaginary which means that the wave is evanescent and does not propagate. The plasma frequency is the cut-off frequency below which a material becomes intransparent. For metals, ω_p is in the ultraviolet regime which is why they strongly reflect visible and infrared light but can be penetrated with X-radiation.

Fig. 2.4 gives a comparison between experimental values for the dielectric functions of silver and gold. We can see that for silver the energy needed to promote electrons from the d-band to states above the Fermi energy is much higher at ≈ 3.7 eV (335 nm). For gold, the transition energy is about 2 eV (620 nm), which leads to strong plasmon damping and the absorption of blue light resulting in the golden color (see i.e. [LHPAD04] for the band structure). This will be important later on when studying the plasmonic mode spectrum.

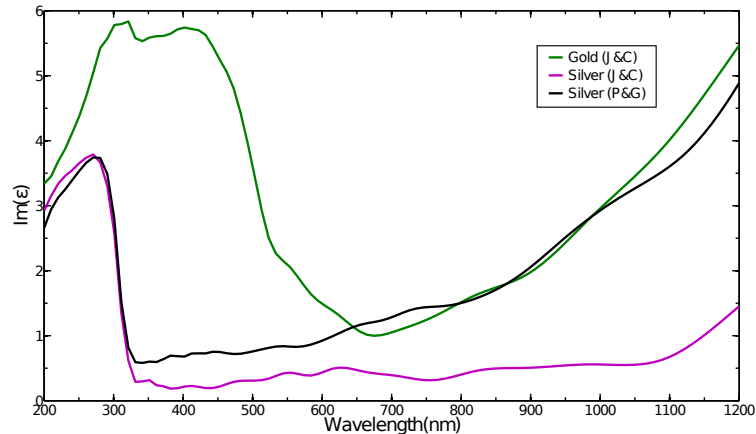


Fig. 2.4: Imaginary part of the dielectric function of gold and silver (obtained via experiments). The energy needed to promote electrons from the d-band to higher states is larger for silver than it is for gold.

2.3 Nano optics

2.3.1 Classical versus quantum approach

To apply a macroscopic description we need to average over a larger region of clustered atoms as their electromagnetic fields fluctuate rapidly. Nanoparticles are somewhat in between the micro- and the macrocosm. They are much smaller than the particles we handle in our everyday life but can still consist of millions of atoms. Metallic nanoparticles do in fact exhibit true quantum mechanical behavior as demonstrated in [AvEW02] for example. However, for macroscopic phenomena we justify to switch to Maxwell's theory as the classical limit of quantum electrodynamics because even for a very distant light source the number of emitted photons is incredibly large. The experimental setups to actually measure what we calculate in this work are not sensible to single photons but rather show the response of the metallic nanoparticles as continuous macroscopic observables. We hide the quantum mechanical properties in the dielectric function which is obtained experimentally. But, if the particles were even smaller and closer together than in this work, this topic should be given further thought. In [ZPN09] the authors state that quantum effects become important for dimer separations below 1 nm. For our purpose, however, we assume that the particles are large enough and make use of Maxwell's macroscopic theory exclusively.

2.3.2 Lifetime and decay rates of an emitter

Once again we use the picture of a harmonically oscillating dipole to obtain the classical lifetime and decay rates of an emitter. The oscillating dipole radiates energy and thus the dipole moment decreases. We want to know when the dipole's energy has decreased by the factor 1/e.

Let us solve the equation of motion for an undriven harmonically oscillating dipole explicitly:

$$\frac{\partial^2}{\partial t^2} \mathbf{r}(t) + \gamma_0 \frac{\partial}{\partial t} \mathbf{r}(t) + \omega_0^2 \mathbf{r}(t) = 0, \quad (2.32)$$

$$\Rightarrow \mathbf{r}(t) = \Re \{ \mathbf{r}_0 \exp \left(-\omega_0 \sqrt{1 - (\gamma_0^2/4\omega_0^2)} t \right) \exp(\gamma_0 t/2) \}. \quad (2.33)$$

To be able to speak of an average dipole energy at any time we must require that $\gamma_0 \ll \omega_0$ in order not to have any problems with decreasing strength of the dipole within one period of oscillation.

The average energy as the sum of the average kinetic and potential energy can be expressed as:

$$\bar{W}(t) = \frac{m\omega_0^2}{2q^2} |\mathbf{r}_0|^2 e^{-\gamma_0 t}, \quad (2.34)$$

with m and q being mass and charge respectively. If τ_0 is the lifetime, defined as the time it takes the oscillator to be at 1/e times its initial energy, it can be seen that

2 Theoretical principles

$$\tau_0 = 1/\gamma_0. \quad (2.35)$$

Energy conservation dictates that

$$\bar{W}(t=0) - \bar{W}(t) = q_i \int_0^t dt' P_0(t'), \quad (2.36)$$

where the “intrinsic quantum yield” q_i has been introduced as a value between zero and one indicating how much of the energy loss is due to radiation. With the average radiated power P_0 in free space [NH06, p. 265]

$$P_0(t) = \frac{|\mathbf{r}(t)|^2}{4\pi\varepsilon_0} \frac{\omega_0^4}{3c^3}, \quad (2.37)$$

it is straight-forward to obtain the atomic decay rate to be:

$$\gamma_0 = q_i \frac{1}{4\pi\varepsilon_0} \frac{2q^2\omega_0^2}{3mc^3}. \quad (2.38)$$

We can note the following: The decay rate depends on the particle’s oscillation frequency, mass and charge and is shorter in media with high indices.

It can be argued that the decay rate corresponds with the radiative linewidth $\Delta\omega \approx \gamma_0$ in agreement with the Lorentzian lineshape function. For details to this and for the case of an inhomogeneous environment consult [NH06, p. 280ff].

2.3.3 Quantum yield

The quantum yield measures how much of the energy dissipated after an excitation event is relaxed radiatively – often wished to be as high as possible – and how much goes to other channels such as vibration, interaction with the environment or quenching. Thus, the quantum yield is defined as:

$$Q = \frac{\gamma_r}{\gamma_r + \gamma_{nr}}, \quad (2.39)$$

with γ_r and γ_{nr} being the radiative and non-radiative decay rates, respectively.

For the homogeneous environment discussed in the previous section 2.3.2 it is identical to the intrinsic quantum yield q_i . For a general environment the total decay rate γ can be split into a sum of radiative and non-radiative parts $\gamma = \gamma_r + \gamma_{nr}$ that can be determined by checking how much of the radiation is transported to the far-field and how much is absorbed in the environment. For example, an emitter sitting close to a golden particle can either be close enough to transfer most of its energy to the particle thus increasing γ_{nr} , or it is a little further out and the presence of the metal surface can increase γ_r strongly.

2.3.4 Cross sections

When traveling light hits a medium energy can be removed in two ways, namely *scattering* and *absorption*. These terms will be used in the way that the total attenuation the light beam experiences is called *extinction* and is the sum of scattering and absorption processes. The scattering cross section is understood to be the power of the scattered electric field integrated over a sphere enclosing the particle divided by the power of the incoming field.

We will neglect all quantum transitions and assume the scattered light to have the same frequency as the incoming light. Furthermore, the particles are treated as independent⁷ and scattering individually, meaning that particles are scattering only the direct light beam and not diffuse light scattered by particles nearby.

Basically, there are three types of particles for which different computation methods can be applied: particles special by their size, spheres with arbitrary size and other geometric forms.

Rayleigh scattering

Let us first look at an elastic scattering process that is valid in the quasistatic regime as discussed in section 2.2.2, that is, a homogeneous electric field is assumed.

The polarizability tensor α is defined by the induced dipole moment \mathbf{p} driven by an external electric field \mathbf{E}_0 via:

$$\mathbf{p} = \alpha \mathbf{E}_0. \quad (2.40)$$

For an incident planar wave $\mathbf{E}_0 e^{-i\omega t}$ the components of α may be complex and dependent on ω . If this incoming wave excites a dipole \mathbf{d} it will radiate in all directions, known as *Rayleigh scattering*. Let \mathbf{P} be a point distant from the particle and γ the angle enclosed by \mathbf{P} and \mathbf{d} (Fig. 2.5).

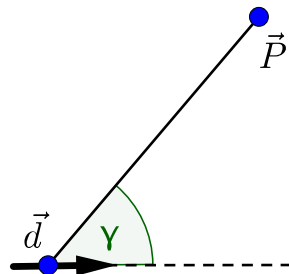


Fig. 2.5: Sketch of a dipole \mathbf{d} that scatters a wave to point \mathbf{P} .

Then the electric field of the scattered wave at the point \mathbf{P} reads:

⁷Particles can safely be considered independent if they are further apart than three times their radii.

2 Theoretical principles

$$E_{\text{sca}} = \frac{k^2 |\mathbf{d}| \sin \gamma}{|\mathbf{r}|} e^{-ik|\mathbf{r}|} \cdot \hat{\mathbf{n}}_e, \quad (2.41)$$

where $\hat{\mathbf{n}}_e$ is perpendicular to $\overline{\mathbf{dP}}$.

The energy flux of the electromagnetic wave is given by the Poynting vector

$$\mathbf{S} = \frac{c}{4\pi} \mathbf{E} \times \mathbf{B}. \quad (2.42)$$

The time average of the energy flux calculates the *intensity* I :

$$\langle S \rangle \equiv I = \frac{c}{8\pi} |\mathbf{E}|^2. \quad (2.43)$$

The total scattered energy in all directions is found by integrating I over a sphere:

$$W_{\text{sca}} = \frac{1}{3} k^4 c |\mathbf{d}|^2. \quad (2.44)$$

Dividing this by the intensity of the incoming wave and normalizing to $|\mathbf{E}_0|$ yields the scattering cross section C_{sca} :

$$C_{\text{sca}} = \frac{8}{3} \pi k^4 |\mathbf{d}|^2. \quad (2.45)$$

The absorption cross section C_{abs} can be found through a similar but mathematically more complex integral over the total intensity as the superposition of the intensity of the incoming and the scattered field and calculates to [vdH81]:

$$C_{\text{abs}} = 4\pi k \Im \left\{ \frac{\mathbf{E}_0}{|\mathbf{E}_0|} \cdot \mathbf{d} \right\}. \quad (2.46)$$

As mentioned above, the extinction is understood to be the sum of scattering and absorption:

$$C_{\text{ext}} = C_{\text{sca}} + C_{\text{abs}}. \quad (2.47)$$

Mie theory

The solution of Maxwell's equations (2.1) allows us to analytically calculate the scattered wave within Mie theory for spheres and by extension for ellipsoids within Mie-Gans theory. A rigorous mathematical derivation can be found in [vdH81] and a summary in [Trü11]; here we only show the final expression for the scattered wave

outside of the particle in spherical coordinates from which the various cross sections can be calculated:

$$u = e^{-\omega t} \cos \varphi \sum_{l=1}^{\infty} a_l r^l \frac{2l+1}{l(l+1)} P_l^1(\cos \theta) h_l^{(2)}(kr), \quad (2.48a)$$

$$v = e^{-\omega t} \sin \varphi \sum_{l=1}^{\infty} b_l r^l \frac{2l+1}{l(l+1)} P_l^1(\cos \theta) h_l^{(2)}(kr), \quad (2.48b)$$

with the Mie scattering coefficients

$$a_l = \frac{n^2 \psi(nx) \psi'_l(x) - \psi_l(x) \psi'_l(nx)}{n^2 \psi_l(nx) \xi'_l(x) - \xi_l(x) \psi'_l(nx)}, \quad (2.49a)$$

$$b_l = \frac{\psi_l(nx) \psi'_l(x) - n \psi_l(x) \psi'_l(nx)}{\psi_l(nx) \xi'_l(x) - n \xi_l(x) \psi'_l(nx)}, \quad (2.49b)$$

and the generating functions

$$\psi_{lm} = \begin{cases} \cos(m\varphi) P_l^m \cos \theta h_l(kr), & \text{even solution} \\ \sin(m\varphi) P_l^m \cos \theta h_l(kr), & \text{odd solution} \end{cases}. \quad (2.50)$$

P_l^m are the associated Legendre functions of first kind, z_l stands for any of the four Bessel functions j_l , y_l , $h_l^{(1)}$ or $h_l^{(2)}$, ψ and ξ are the Riccati-Bessel functions and n is the refractive index.

Cross sections with the Boundary Element Method

There are various numerical approaches to arbitrary particle shapes like the popular Discrete Dipole Approximation [DF94] or our choice, the Boundary Element Method as introduced in section 2.2.5. Once the electric field has been calculated we can connect the cross sections to the Poynting vector (2.42) via the optical theorem [Jac98, p. 501]:

$$C_{\text{sca}} = n_b \int_{\partial\Omega} da \Re\{\hat{\mathbf{n}} \cdot (\mathbf{E} \times \mathbf{B}^*)\}, \quad (2.51)$$

$$C_{\text{ext}} = -\frac{1}{n_b} \int_{\partial\Omega} da \Re\{\hat{\mathbf{n}} \cdot (\mathbf{E} \times \mathbf{B}_0^* + \mathbf{E}_0^* \times \mathbf{B})\}, \quad (2.52)$$

$$C_{\text{abs}} = C_{\text{ext}} - C_{\text{sca}}, \quad (2.53)$$

where n_b is the refractive index and $\hat{\mathbf{n}}$ a normal vector to the surface as in previous sections. Experimentally, the absorption cross section might be easiest to measure because one only has to check how much of an incoming beam is absorbed in the direction of impact.

2.3.5 Energy transfer between quantum emitters

There is a mechanism that allows for radiationless energy transfer; the most prominent example is probably the energy transfer between proteins in photosynthesis. The absorbed energy of light has to be transferred over longer distances to the reaction center where it is used for a charge separation.

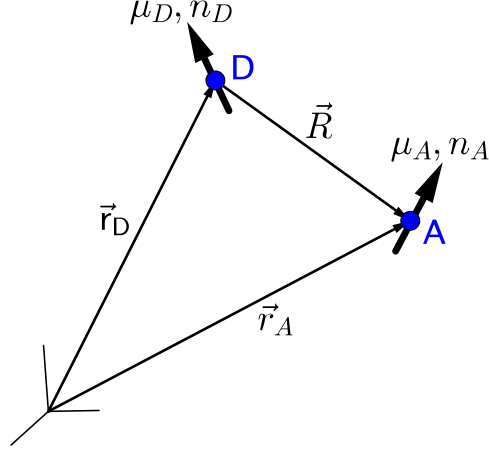


Fig. 2.6: Two dipoles are situated next to each other separated by the distance $|\mathbf{R}|$ and act as energy donor **D** and acceptor **A**.

This can be understood in a semi-classical picture where the donor and acceptor molecules have distinct energy levels. Let **D** and **A** be a donor and an acceptor separated by the distance \mathbf{R} and μ_D and μ_A their dipole moments (Fig. 2.6). Connecting the classical with the quantum mechanical picture we can generally say that [NH06, Sec. 8.5f.]:

$$\frac{\gamma_{D \rightarrow A}}{\gamma_0} = \frac{P_{D \rightarrow A}}{P_0}, \quad (2.54)$$

where $\gamma_{D \rightarrow A}$ is the energy transfer rate from donor to acceptor and γ_0 is the donor's decay rate if no acceptor is present. $P_{D \rightarrow A}$ denotes the donor's energy (per unit time) that is absorbed by the acceptor and P_0 is the energy the donor releases in absence of an acceptor. Picturing a radiating dipole for the donor, the expressions for γ_0 and P_0 are known ([NH06, p. 278, p. 286]) and we need to calculate $P_{D \rightarrow A}$. The transferred power reads according to Poynting's theorem as:

$$P_{D \rightarrow A} = -\frac{1}{2} \int_{V_A} dV \Re \{ \mathbf{j}_A^* \cdot \mathbf{E}_D \}, \quad (2.55)$$

where \mathbf{j}_A is the current density associated with the charges of the acceptor which is

in the dipole approximation⁸ given by $\mathbf{j}_A = -\imath\omega_0\boldsymbol{\mu}_A\delta(\mathbf{r} - \mathbf{r}_A)$. This leads to:

$$P_{D \rightarrow A} = \frac{\omega_0}{2} \Im\{\boldsymbol{\mu}_A^* \cdot \mathbf{E}_d(\mathbf{r}_A)\}. \quad (2.56)$$

By acknowledging that $\boldsymbol{\mu}_A$ is a dipole moment *induced* by the donor's field we can use the polarizability tensor α_A as in equation (2.40) to express the dipole moment $\boldsymbol{\mu}_A$. Assuming the acceptor can only be polarized in the direction of $\boldsymbol{\mu}_A$ the power transfer can then be rewritten as:

$$P_{D \rightarrow A} = \frac{\omega_0}{2} \Im\{\alpha_A\} |\hat{\mathbf{n}}_A \cdot \mathbf{E}_D(\mathbf{r}_A)|^2. \quad (2.57)$$

This connects the energy absorption to the imaginary part of the polarizability and the electric field projected on the dipole axis.

As briefly seen in section 2.3.4 the absorption cross section C_{abs} can replace the polarizability α in the description. Furthermore, calculating the spherical integral over the power of the scattered electric field yields:

$$P_{D \rightarrow A} = \frac{3}{2} \sqrt{\frac{\varepsilon_0}{\mu_0}} n(\omega_0) C_{abs,A}(\omega_0) |\hat{\mathbf{n}}_A \cdot \mathbf{E}_D(\mathbf{r}_A)|^2. \quad (2.58)$$

The donor's field \mathbf{E}_D at the acceptor's position \mathbf{r}_A can be expressed via the Green function:

$$\mathbf{E}_D(\mathbf{r}_A) = \omega_0^2 \mu_0 G(\mathbf{r}_A, \mathbf{r}_D) \boldsymbol{\mu}_D. \quad (2.59)$$

By substituting $k(\omega_0) := (\omega_0/c)n(\omega_0)$ we can define a function $T(\omega_0)$ as:

$$T(\omega_0) = 16\pi^2 k^2 R^6 |\hat{\mathbf{n}}_A \cdot G(\mathbf{r}_A, \mathbf{r}_D) \hat{\mathbf{n}}_D|^2, \quad (2.60)$$

with $R := \mathbf{r}_D - \mathbf{r}_A$. This function is basically what we are interested in, and by using the above it follows for the normalized transfer rate:

$$\frac{\gamma_{D \rightarrow A}}{\gamma_0} = \frac{9c^4}{8\pi R^6} \frac{C_{abs,A}(\omega_0)}{n^4(\omega_0)\omega_0^4} T(\omega_0). \quad (2.61)$$

By rewriting this with an integral over the Dirac delta function $\delta(\omega - \omega_0)$ and recognizing that the donor emits over a range of frequencies we arrive at:

$$\frac{\gamma_{D \rightarrow A}}{\gamma_0} = \frac{9c^4}{8\pi R^6} \int_0^\infty d\omega \frac{f_D(\omega) C_{abs,A}(\omega)}{n^4(\omega)\omega^4} T(\omega), \quad (2.62)$$

where $f_D(\omega)$ is the donor's normalized emission spectrum in a medium with $n(\omega)$ as index.

This tells us that the transfer rate depends on the spectral overlap of the donor's emission spectrum and the acceptor's absorption cross section.

⁸The dipole approximation truncates the power expansion for E after the second term which is justified by having the two dipoles that simulate a quantized two-level system be closer to each other than the wavelength of the impinging wave, see [NH06, Sec. 13.3].

2 Theoretical principles

In Fig. 2.7, $T(\omega)$ is plotted as a function of the distance R between donor and acceptor. Differently aligned dipoles are used to show that the behavior depends on the dipoles' orientations. For all orientations the short distance behavior of T is constant, therefore $\gamma_{D \rightarrow A}$ scales as R^{-6} (Förster type energy transfer). If the dipoles are aligned, the long distant behavior for T scales as R^2 and therefore $\gamma_{D \rightarrow A}$ decays as R^{-4} . If the dipoles are not aligned, $T(\omega)$ is proportional to R^4 making $\gamma_{D \rightarrow A}$ decay with R^{-2} .

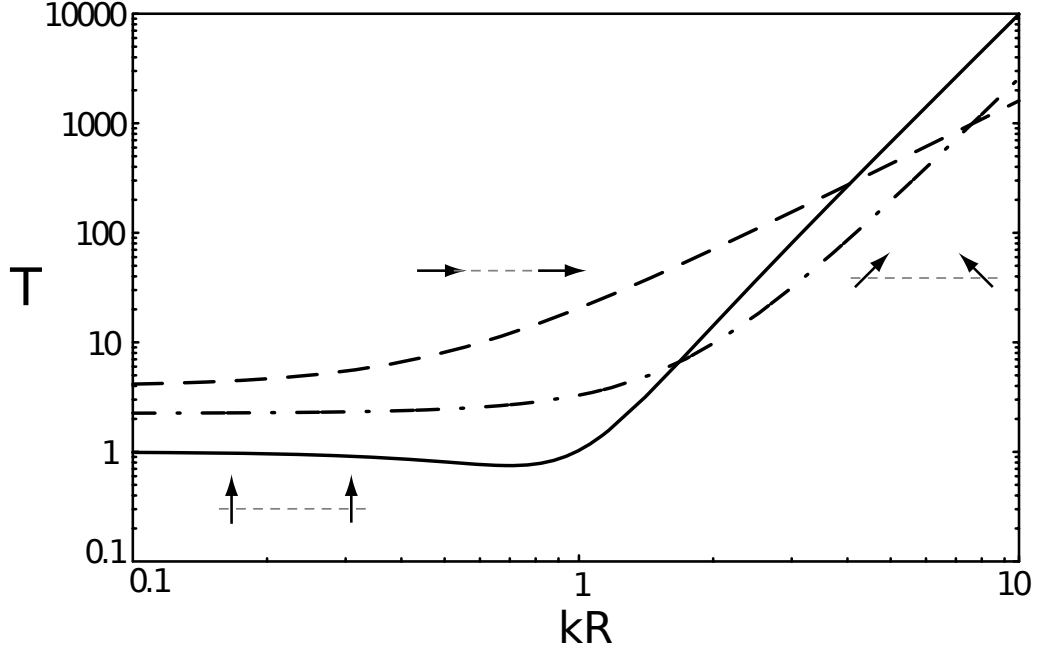


Fig. 2.7: Dependence of $T(\omega)$ on the distance separating donor and acceptor for different dipole orientations.

Taken from: [NH06]

2.4 Plasmons

Plasmons are the quasiparticles of surface charge density oscillations; or classically the collective oscillations of electron gas density. They can be categorized by their location in bulk, particle and surface plasmons, and we will see that the dielectric function as investigated in section 2.2.7 plays a crucial role. Since most phenomena can be derived by picturing plasmons as classical quantized plasma oscillations our starting point will once again be the Maxwell equations. For a lengthy discussion see e.g. [Mai07].

2.4.1 Surface plasmons

Let us investigate how plasmons can occur at surfaces, i.e. at intersections of different media. As seen in section 2.2.1 all electromagnetic waves have to obey the Helmholtz equation

$$(\nabla^2 + \varepsilon(\omega)k^2)\mathbf{E}(\mathbf{r}, \omega) = 0. \quad (2.2a)$$

We assume the following setup: a planar interface in the xy-plane separates a metal from a dielectric. Thus, for $z < 0$ the metal has a complex dielectric function $\varepsilon_1(\omega)$ and for $z > 0$ the dielectric has a real dielectric function $\varepsilon_2(\omega)$. We now have to solve the wave equation (2.2a) for both regions (in each of which $\varepsilon(\omega)$ is spatially constant) and connect the solutions with appropriate boundary conditions.

Principally, two sets of solutions can be found for the Maxwell equations manifesting in different light polarizations. The light can either be polarized perpendicularly (“p”- resp. “TM”-polarized) or transversally (“s”- resp. “TE”-polarized) in respect to the electric field. Plasmons cannot be excited with TE-polarized light [Mai07, p. 26f.] which is why we can propose a TM-polarized solution of the wave equation as:

$$\mathbf{E}_j = \begin{pmatrix} E_{j,x} \\ 0 \\ E_{j,z} \end{pmatrix} e^{ik_x x - i\omega t} e^{ik_{j,z} z}. \quad (2.63)$$

$j = 1, 2$ denotes medium 1 or 2. The parallel component of the wave vector k_x is conserved and thus the same for both media, giving:

$$k_x^2 + k_{j,z}^2 = \varepsilon_j k^2, \quad (2.64)$$

with $k = 2\pi/\lambda$. Using Gauss’ law (2.1a) it follows that:

$$k_x E_{j,x} + k_{j,z} E_{j,z} = 0. \quad (2.65)$$

Inserting this in our ansatz (2.63) yields:

$$\mathbf{E}_j = E_{j,x} \begin{pmatrix} 1 \\ 0 \\ -k_x/k_{j,z} \end{pmatrix} e^{ik_x x - i\omega t} e^{ik_{j,z} z}. \quad (2.66)$$

For the interface we use the boundary conditions for the electric field as motivated in section 2.2.4:

$$E_{1,x} - E_{2,x} = 0, \quad (2.67a)$$

$$\varepsilon_1 E_{1,z} - \varepsilon_2 E_{2,z} = 0. \quad (2.67b)$$

The set of equations (2.65) together with (2.67) has two solutions. For the trivial case $k_x = 0$ obviously no wave propagates which leaves us with:

2 Theoretical principles

$$\varepsilon_1 k_{2,z} - \varepsilon_2 k_{1,z} = 0. \quad (2.68)$$

Using equation (2.64) we directly arrive at the dispersion relation between k and ω :

$$k_x = \frac{\omega}{c} \sqrt{\frac{\varepsilon_1 \varepsilon_2}{\varepsilon_1 + \varepsilon_2}}, \quad (2.69a)$$

$$k_{j,z} = \frac{\omega}{c} \sqrt{\frac{\varepsilon_j^2}{\varepsilon_1 + \varepsilon_2}}. \quad (2.69b)$$

For the wave we are looking for we require two constraints. Namely that the wave can actually propagate along the surface (implying a real k_x) and that it does not propagate into the medium (implying an imaginary $k_{j,z}$ to get an evanescent, i.e. exponentially decaying field in z -direction):

$$\varepsilon_1 \varepsilon_2 < 0, \quad (2.70a)$$

$$\varepsilon_1 + \varepsilon_2 < 0. \quad (2.70b)$$

This can be achieved by having for example a noble metal such as gold or silver inside air or vacuum, like we have assumed from the beginning.

2.4.2 Particle plasmons

Thus far we have looked at surface plasmons which are confined to an infinite plane. Particle plasmons are surface plasmons confined to a closed surface such as a metallic nanoparticle. The free electron gas gets polarized and the particle acts as an oscillator (Fig. 2.8).

This can be pictured as bending a plane along which surface plasmons propagate into a closed shape. Then, surface plasmons must form standing waves in analogy to Bohr's atom model where the de Broglie wavelength of the electron must do just that. In this sense, light is confined to a nanoscale particle.

The most intuitive mode is the dipole mode as pictured in Fig. 2.8. For spheres and in the quasistatic approximation the solution of the Laplace equation is given by ([Jac98, p. 101]):

$$\Phi(r, \theta) = \sum_{l=0}^{\infty} (A_l r^l + B_l r^{-(l+1)}) P_l(\cos \theta), \quad (2.71)$$

with θ being the angle between the z-axis and the position r and $P_l(\cos \theta)$ the Legendre polynomials. The solution can be split up for potentials inside and outside the sphere and the coefficients A_l and B_l are determined from the boundary conditions,

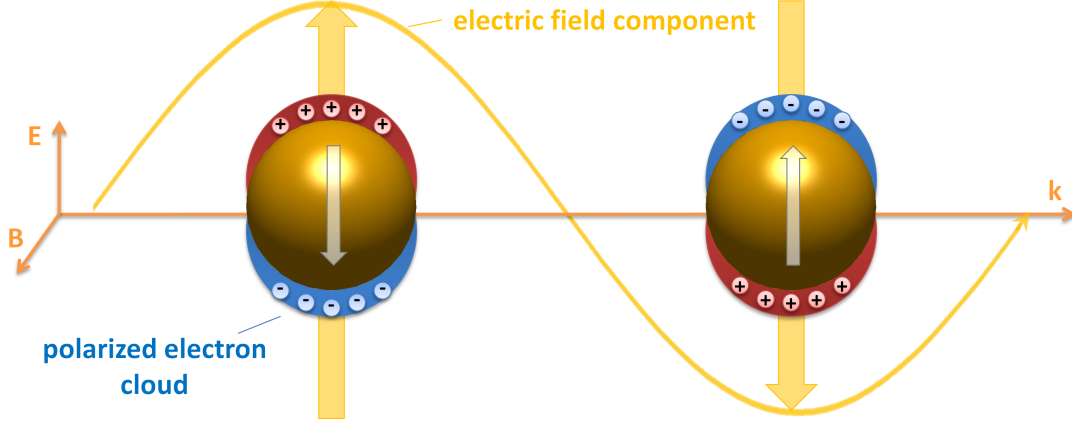


Fig. 2.8: An electromagnetic wave polarizes the electron gas of a metallic particle forming a particle plasmon.

Taken from: [Trü11]

giving for a sphere with radius a and dielectric function $\varepsilon(\omega)$ in a medium with the dielectric function ε_m [Mai07, p. 67]:

$$\Phi_{\text{in}} = \frac{3\varepsilon_m}{\varepsilon + 2\varepsilon_m} E_0 r \cos \theta, \quad (2.72a)$$

$$\Phi_{\text{out}} = -E_0 r \cos \theta + \frac{\varepsilon - \varepsilon_m}{\varepsilon + 2\varepsilon_m} E_0 a^3 \frac{\cos \theta}{r^2}. \quad (2.72b)$$

Note that equation 2.72b describes the superposition of the applied electric field and a dipole field from an emitter at the center of the sphere. Defining the dipole moment \mathbf{p} as

$$\mathbf{p} = 4\pi\varepsilon_0\varepsilon_m a^3 \frac{\varepsilon - \varepsilon_m}{\varepsilon + 2\varepsilon_m} \mathbf{E}_0 \quad (2.73)$$

we can rewrite the potential outside the sphere as

$$\Phi_{\text{out}} = -E_0 r \cos \theta + \frac{\mathbf{p} \cdot \mathbf{r}}{4\pi\varepsilon_0\varepsilon_m r^3}. \quad (2.74)$$

The polarizability α is connected to \mathbf{p} via $\mathbf{p} = \varepsilon_0\varepsilon_m\alpha\mathbf{E}_0$ which results in:

$$\alpha = 4\pi a^3 \frac{\varepsilon - \varepsilon_m}{\varepsilon + 2\varepsilon_m}. \quad (2.75)$$

The polarizability α is maximal for a minimal denominator $|\varepsilon + 2\varepsilon_m|$, or, assuming a practically constant imaginary part of $\varepsilon(\omega)$ around the resonance:

$$\Re\{\varepsilon(\omega)\} = -2\varepsilon_m. \quad (2.76)$$

2 Theoretical principles

This is called the *Fröhlich condition* constituting the dipole surface plasmon for a metallic nanoparticle. In the Drude model and for $\varepsilon_m = 1$ (air), this condition is met for $\omega_0 = \omega_p/\sqrt{3}$.

In this calculation only the first order Legendre polynomials contributed to the solution to arrive at the dipole mode. Considering $l > 1$, higher orders with no net dipole moment follow.

2.4.3 Bulk plasmons

If the electrons of a metal are displaced at once then the ions act as restoring force establishing an oscillation with the plasma frequency, the quasiparticle of which is called a *bulk plasmon*. Due to the longitudinal nature of the oscillation this cannot be accomplished by a transversal electromagnetic wave; bulk plasmons have to be excited by impact of a charged particle [Mai07, p. 16].

2.4.4 Excitation of plasmons

Let's have a look at the surface plasmon dispersion relation (2.69a) and the light line $\omega = ck_x$.

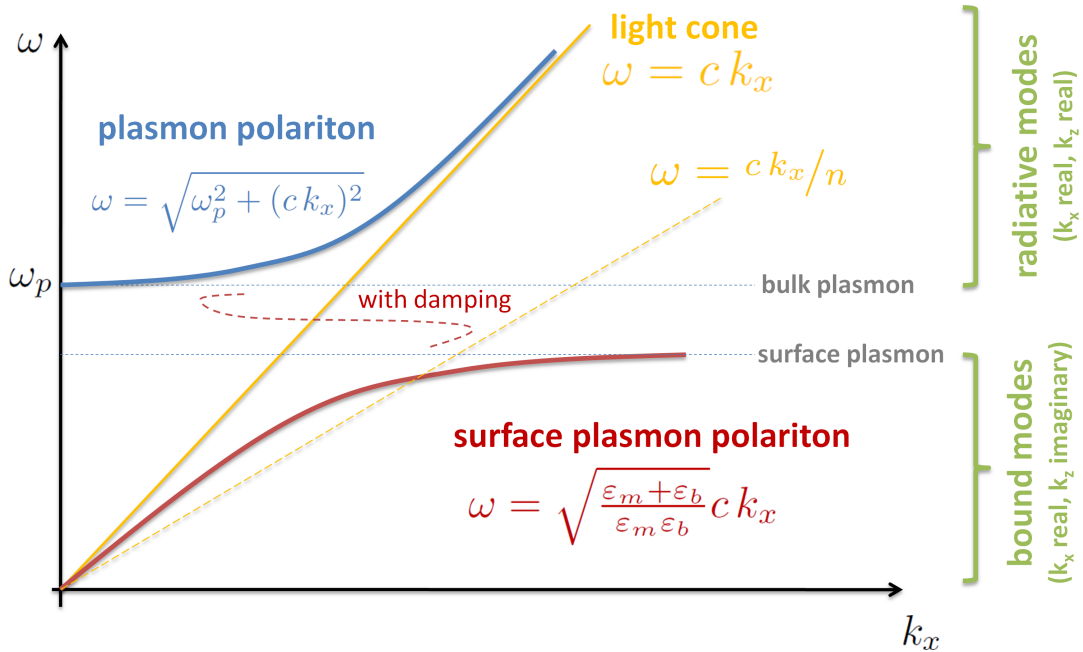


Fig. 2.9: Dispersion relation for a surface plasmon. The light line has to be tilted by using a dielectric with refractive index $n > 1$ in order to be able to excite a plasmon.

Taken from: [Trü11]

We can see in Fig. 2.9 that the light line (yellow) does never cross the dispersion line of a surface plasmon (red). A light wave lacks the necessary momentum to excite a plasmon. However, the light line can easily be tilted by having the light travel through a medium with a refractive index greater than one (dashed line).

Two experimental setups can accomplish this by using evanescent waves that are generated at an interface, namely the “*Otto*” configuration and the “*Kretschmann*” configuration [NH06, p. 389].

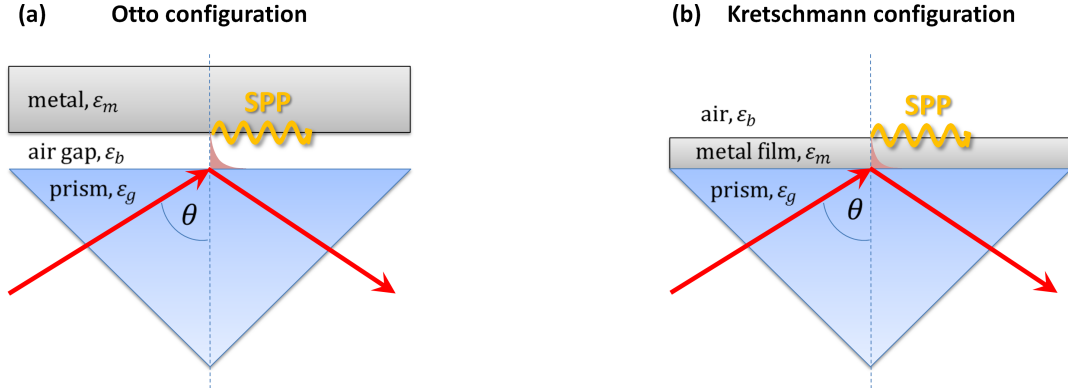


Fig. 2.10: (a) Otto configuration and (b) Kretschmann configuration for tilting the light line to be able to excite surface plasmons.

Taken from: [Trü11]

The left side of Fig. 2.10 shows the Otto configuration where a prism is kept at a constant distance from the metal surface. The total reflection at the interface between the prism and the (air) gap generates an evanescent field which can excite a surface plasmon at the metal surface that follows the gap.

The right side sketches the Kretschmann configuration where the prism is directly put into contact with the metal. The evanescent field penetrates the metal and can excite a surface plasmon at the other side of the metal, i.e. the surface between the metal and the surrounding medium, providing the skin depth is sufficient [Trü11, p. 16].

2.5 Plasmons confined to nanoparticles

In this section we will investigate the different kinds of standing waves that can be established for a metallic nanoparticle focussing on disc shapes.

2.5.1 Surface and edge modes

Generally we can distinguish between surface (or film) modes and edge modes which are classified by their symmetry. While surface modes possess a radial symmetry, edge modes exhibit azimuthal symmetry. We will use a notation seen in [SDH⁺12]

2 Theoretical principles

which follows the classification of mechanical vibrations according to the number of radial and azimuthal node lines ($\#R, \#A$).

Let us look at representative modes that can be excited in a metallic nanodisc.

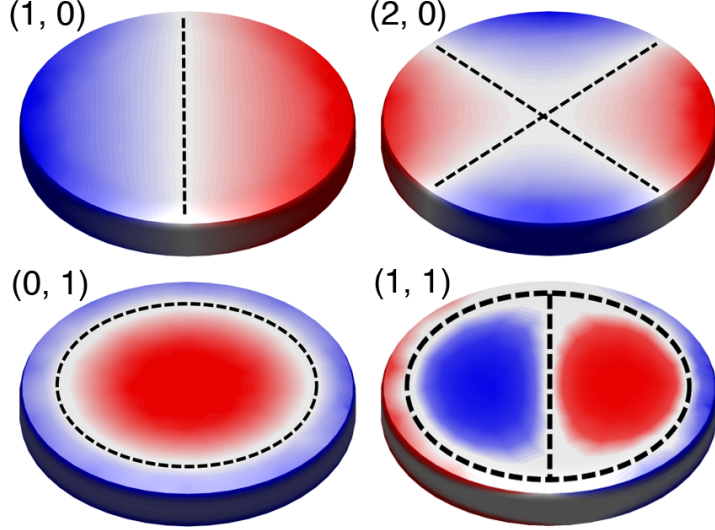


Fig. 2.11: Two multipole modes, the breathing mode and the hybrid double breathing mode with radial and/or azimuthal node lines (dashed) constituting fundamentally different types of oscillations.

Fig. 2.11 shows two multipole modes, namely the well-known *dipole mode* (1, 0) and the *quadrupole mode* (2, 0). Dashed lines indicate the associated radial node lines. Mode (0, 1) is structurally different as it exhibits an azimuthal node line while mode (1, 1) is a hybrid mode with both a radial and an azimuthal node line. It will be descriptively named “*double breathing mode*” in this work. The wavelength of the standing wave has to fit into such a node line.

Mode (0, 1) is of particular interest in this work and will be introduced in the following section.

2.5.2 Breathing modes

Because of its remarkable symmetry and the oscillation of electron densities between the center and the edge of the disc, mode (0, 1) was named *breathing mode* [SDH⁺12]. It has only recently been discovered in electron energy loss spectroscopy measurements (see section 3.1.3), and its optical properties are a central part of this work.

As with multipole modes (dipole, quadrupole, hexapole, . . .), higher orders of this type of oscillation exist.

2.5.3 Bright and dark plasmonic modes

Parallel to the classification by node lines a further type is useful that stems from the optical visibility of a certain mode. An incoming plane light wave cannot excite modes with no net dipole moment because of the inherent symmetry of the system. This is why the dipole mode is dominant and the breathing mode especially has remained optically hidden thus far.

The following chapter is dedicated to introducing the main idea of this work, which is to break the symmetry of an optical system in order to make “dark” modes accessible for optical experiments, i.e. a light wave. Also, two other methods are described, namely the excitation by an oscillating dipole and the excitation by an electron beam.

3 Plasmon simulation

3.1 Imaging of plasmons

Conventional mapping of surface plasmons is not possible due to the Abbe diffraction limit of light [NH06, p. 97]. In the past years powerful techniques have been developed to overcome this limit such as scanning of the near field or confocal microscopy.

In this chapter we will have a look at three different types of external excitations, namely by a *plane wave*, an *oscillating dipole* and an *electron beam*, and how plasmons can be made visually accessible for the three of them.

3.1.1 Plane wave excitation

By looking at what a particle plasmon is in section 2.4.2 it can be intuitively understood how an incident electromagnetic wave can excite such an oscillator's dipole mode. The electric field forces electrons to move to one side of the particle thus polarizing the electron cloud which is set in motion by the arising restoring force.

The crux is that because of the symmetry of the incident wave the electric field is more or less constant throughout the particle and especially at its borders.

However, we can overcome this limitation by acknowledging that only one of the particle's dimensions has to be large enough to encapsulate a sufficiently large part of the wavelength to bring retardation effects into play if the incoming light is simply tilted [HLA⁺08].

For disc-shaped nanoparticles this is certainly the case as one dimension (the diameter) exceeds the other (the height) by an arbitrarily large factor. When light hits the disc perpendicular to its dominant surface the small path inside the particle is not enough to provide an alternating electric field. On the other hand, if the light beam is tilted such that it can penetrate the particle along its longest axis then the symmetry is broken and electrons can for example be pushed into the corners of the disc (Fig. 3.1).

Thus, scattering measurements can show “dark” plasmonic modes by using light at oblique angles.

3.1.2 Dipole excitation

In section 2.3.5 we have discussed that energy can be transferred from a donating to an accepting molecule and have given an expression for the energy transfer rate (2.62).

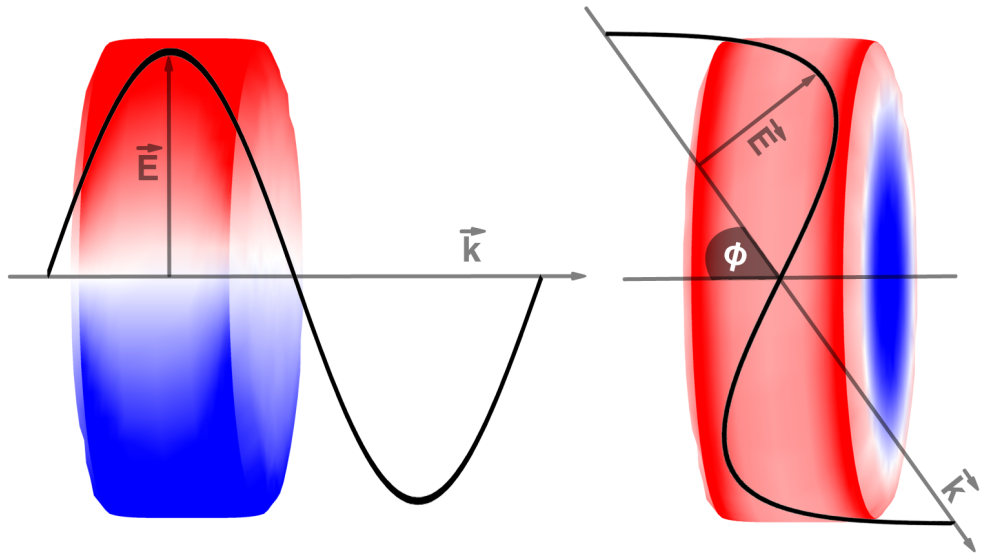


Fig. 3.1: Tilting the wave vector fits more of a wavelength into the particle, and the electric field is not constant for opposing sides of the disc. Electrons are pushed into the corners of the particle allowing modes with no dipole moment to be excited.

In free space, the transfer rate behaves differently for the *near field* and for the *far field*. The near field is roughly the region enclosed by the distance of one wavelength around the emitter. The transfer rate to an acceptor close to the donor is proportional to R^{-6} due to Coulomb interaction. In the far field, i.e. further out than approximately one wavelength, the dependence is R^{-2} , pictured as the emission and reabsorption of photons.

This behavior can change drastically when a metallic nanoparticle is brought into play. The field the molecules experience is modified in a way that allows for transfer rates to be changed by the order of magnitudes. The molecules can use the nanoparticle as an “antenna” to emit and absorb energy. A demonstrated example of tuned nanodiscs is [GRH⁺07] where fluorophores were put on nanodisc arrays. The molecules absorb in the ultraviolet and emit in the visible regime which allows the separation of excitation and emission channels (Fig. 3.2). This constitutes an interesting property for technological use, such as sensors or data storage.

The interaction between the molecules (which can be described as emitting dipoles, [NH06, Sec. 13.3]) and the metallic nanoparticle gives rise to the possibility to study the different modes of the nanoparticle that can be excited by a dipole in its vicinity. Very close to the source there are no symmetry restrictions to be fulfilled and arbitrary wave vectors can occur locally, making this case of particular interest to study the

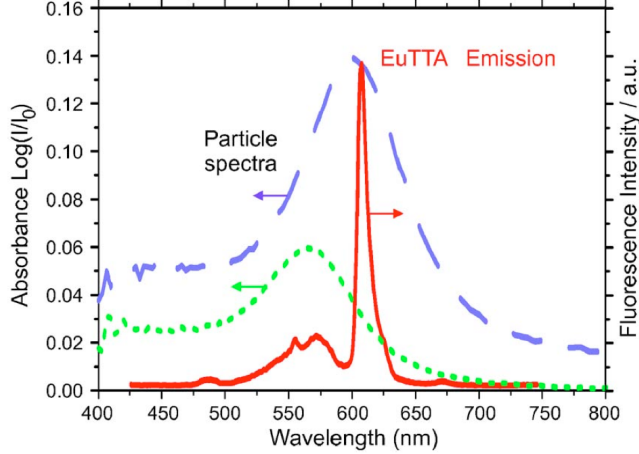


Fig. 3.2: Absorbance spectra for two nanodiscs (dashed and dotted lines) and emission spectrum of fluorophores (solid line).

Taken from: [GRH⁺ 07]

breathing mode.

We closely but briefly follow [HT08] to describe the system of a nanoparticle placed near a molecule.

A two level system is considered for the molecule, which fits well with an experimental realization via quantum dots. The molecule can reach from the ground state 0 the excited state 1 with energy E_1 . We split the dipole operator $\hat{\mathbf{d}}$ into the dipole excitation operator $\hat{\mathbf{d}}^+$ and the dipole relaxation operator $\hat{\mathbf{d}}^-$ and connect them to the molecular excitation operator $\hat{\sigma}_+ = |1\rangle\langle 0|$ and the molecular relaxation operator $\hat{\sigma}_- = |0\rangle\langle 1|$ through the molecular dipole moment μ :

$$\hat{\mathbf{d}} \equiv \hat{\mathbf{d}}^+ + \hat{\mathbf{d}}^- = \mu(\hat{\sigma}_- + \hat{\sigma}_+). \quad (3.1)$$

Representing the free Hamiltonian as $\hat{H}_0 = E_1 |1\rangle\langle 1|$ the molecular operators σ_\pm oscillate with the frequency $e^{\pm\omega t}$, and we split the electric field operator into terms evolving with positive and negative frequencies accordingly:

$$\hat{\mathbf{E}}(\mathbf{r}) = \hat{\mathbf{E}}^+(\mathbf{r}) + \hat{\mathbf{E}}^-(\mathbf{r}). \quad (3.2)$$

Within dipole approximation, the coupling between the molecule and light is described by

$$\hat{H} = -\hat{\mathbf{d}} \cdot \hat{\mathbf{E}} \approx -(\hat{\mathbf{d}}^+ \cdot \hat{\mathbf{E}}^- + \hat{\mathbf{d}}^- \cdot \hat{\mathbf{E}}^+). \quad (3.3)$$

An eigenmode expansion of $\hat{\mathbf{E}}^\pm$ fails in a complex dielectric environment where absorption has to be accounted for but can be avoided by an approach via Green's function.

3 Plasmon simulation

The starting point for this is Fermi's golden rule for the spontaneous emission rate [Fer32] for a molecule at position \mathbf{r}_m :

$$\gamma = 2\pi\mu_i \left\langle \hat{E}_i^+(\mathbf{r}_m, \omega) \hat{E}_j^-(\mathbf{r}_m, \omega) \right\rangle \mu_j. \quad (3.4)$$

The term in brackets describes field fluctuations induced by current noise in the metal.

For a classical current \mathbf{j} the following wave equation holds [Jac98]:

$$\nabla \times \nabla \times \mathbf{E}(\mathbf{r}, \omega) - k^2 \varepsilon(\mathbf{r}, \omega) \mathbf{E}(\mathbf{r}, \omega) = \frac{4\pi i\omega}{c^2} \mathbf{j}(\mathbf{r}, \omega), \quad (3.5)$$

as well as in terms of the dyadic Green tensor:

$$\nabla \times \nabla \times \mathbf{G}(\mathbf{r}, \mathbf{r}', \omega) - k^2 \varepsilon(\mathbf{r}, \omega) \mathbf{G}(\mathbf{r}, \mathbf{r}', \omega) = 4\pi \delta(\mathbf{r} - \mathbf{r}') \mathbb{1}. \quad (3.6)$$

Comparing equation (3.5) with equation (3.6) we observe that if Green's function is available it can serve as the link between the current source and the electric field:

$$\mathbf{E}(\mathbf{r}, \omega) = \frac{i\omega}{c^2} \int d\mathbf{r}' \mathbf{G}(\mathbf{r}, \mathbf{r}', \omega) \mathbf{j}(\mathbf{r}', \omega). \quad (3.7)$$

Equation (3.7) can now be redirected to the corresponding electric field and current operators if $\hat{\mathbf{j}}^\pm$ induces $\hat{\mathbf{E}}^\pm$:

$$\begin{aligned} \left\langle \hat{E}_i^+(\mathbf{r}_m, \omega) \hat{E}_j^-(\mathbf{r}_m, \omega) \right\rangle &= \frac{\omega^2}{c^4} \int d\mathbf{r} d\mathbf{r}' G_{ik}(\mathbf{r}_m, \mathbf{r}, \omega) \\ &\quad \times \left\langle \hat{j}_k^+(\mathbf{r}, \omega) \hat{j}_l^-(\mathbf{r}', \omega) \right\rangle G_{jl}^*(\mathbf{r}_m, \mathbf{r}', \omega). \end{aligned} \quad (3.8)$$

Equation (3.8) relates the field fluctuations to the current fluctuations in the dielectric, and Green's function propagates the current source to the position of the molecule.

By multiplying equation (3.6) with G_{ij}^* and further manipulating it the following integral equation can be obtained:

$$\int ds G_{ik}(\mathbf{r}, \mathbf{s}, \omega) k^2 \varepsilon''(\mathbf{s}, \omega) G_{jk}^*(\mathbf{r}', \mathbf{s}, \omega) = 4\pi \Im \{ G_{ij}(\mathbf{r}, \mathbf{r}', \omega) \}, \quad (3.9)$$

where $\varepsilon''(\omega)$ is the imaginary part of the dielectric function. From Fermi's golden rule together with equations (3.8) and (3.9) we finally arrive at the result

$$\gamma = 2k^2 \boldsymbol{\mu} \cdot \Im \{ \mathbf{G}(\mathbf{r}_m, \mathbf{r}, \omega) \} \cdot \boldsymbol{\mu}, \quad (3.10)$$

which can be made more transparent by going back to equation (3.7) and using $\mathbf{j} = -i\omega \boldsymbol{\mu}$:

$$\frac{\gamma}{2} = -\Im \{ \boldsymbol{\mu} \cdot \mathbf{E}(\mathbf{r}_m) \}. \quad (3.11)$$

The important equation (3.10) shows that the decay rate of a molecule is fully determined by Green's function of classical Electrodynamics, even if a metallic nanoparticle is present. This is a great simplification as all fluctuation dynamics are incorporated in the dielectric function of the metal.

$\mathbf{E}(\mathbf{r}_m)$ is the electric field induced by the dipole $\boldsymbol{\mu}$, and therefore equation (3.11) denotes a self-interaction between the dipole which polarizes the metallic nanoparticle and the field acting back on the dipole. The latter is the sum of the field of the dipole itself and that of the polarized particle. The imaginary part is what's responsible for the decay of the molecule.

Let us sum up the channels energy can flow in a coupled dipole-nanoparticle system. First of all, the emitter in an excited state can relax radiatively by sending photons to the far field and non-radiatively convert energy to heat. Secondly, the presence of the nanoparticle gives rise to quenching, i.e. non-radiative Förster type transfer of energy from the dipole to the nanoparticle where it is again converted to heat or other Ohmic losses. And lastly, the dipole can transfer energy to the nanoparticle that is resonant with plasmonic excitations, which themselves can decay radiatively or non-radiatively.

3.1.3 Electron energy loss spectroscopy

Electron energy loss spectroscopy (EELS) has in recent years become an important technique for mapping plasmonic fields for all kinds of particle shapes. The idea is to send an electron beam of high kinetic energy through or besides a nanoparticle and measure the energy loss it experiences. The following section follows [Hoh14]; for a more in-depth look consider [dA02].

We describe an electron that is sent on its way through or close to a metallic nanoparticle. We will neglect the small velocity change it experiences due to excitations, justified by a much higher kinetic energy than the plasmon energies, which is typically the case.

If the electron travels along $\mathbf{r}(t) = \mathbf{r}_0 + \mathbf{v}t$ in z-direction then the electron charge distribution is given by

$$\rho(\mathbf{r}, \omega) = -e \int dt e^{i\omega t} \delta(\mathbf{r} - \mathbf{r}_0 - \mathbf{v}t) = -\frac{e}{v} \delta(\mathbf{R} - \mathbf{R}_0) e^{iq(z-z_0)}, \quad (3.12)$$

with $v = |\mathbf{v}|$ the velocity of the electron, $-e$ its charge, $q = \omega/v$ the wave number, \mathbf{R}_0 the impact parameter in the xy-plane (two-dimensional coordinates) and \mathbf{R} the xy-position on the plane.

The potentials caused by such a charge in motion are analytically known [Jac98, p. 661ff.] and yield [dA02]:

$$\Phi_{\text{ext}}(\mathbf{r}) = -\frac{2}{v\varepsilon_j} K_0 \left(\frac{q|\mathbf{R} - \mathbf{R}_0|}{\gamma_j} \right) e^{iq(z-z_0)}, \quad (3.13)$$

$$\mathbf{A}_{\text{ext}}(\mathbf{r}) = \varepsilon_j \frac{\mathbf{v}}{c} \Phi_{\text{ext}}(\mathbf{r}), \quad (3.14)$$

3 Plasmon simulation

with K_0 the modified Bessel function and $\gamma_j = (1 - \varepsilon_j v^2/c^2)^{-1/2}$.

Within our BEM approach the proper boundary conditions are automatically fulfilled (see section 2.2.5), and we can directly use equation (3.13) in the equation for the total scalar and vector potential (2.24).

The energy loss can be calculated via the work the electron has to perform against the induced field:

$$\Delta E = e \int dt \mathbf{v} \cdot \mathbf{E}_{\text{ind}}[\mathbf{r}(t), t] = \int_0^\infty d\omega \hbar \omega \Gamma_{\text{EELS}}(\mathbf{R}, \omega). \quad (3.15)$$

Γ_{EELS} is the loss probability per unit of transferred energy and is given by:

$$\Gamma_{\text{EELS}}(\mathbf{R}, \omega) = \frac{e}{\pi \hbar \omega} \int dt \Re \{ e^{-i\omega t} \mathbf{v} \cdot \mathbf{E}_{\text{ind}}[\mathbf{r}(t), \omega] \} + \Gamma_{\text{bulk}}(\omega). \quad (3.16)$$

Γ_{bulk} is the bulk loss probability which, for the quasistatic approximation, is proportional to the propagation length and the loss function $\Im \{-1/\varepsilon(\omega)\}$; for more general purposes we are again referring to [dA02].

Thus, Γ_{EELS} can be computed by calculating the induced electric field along the electron's trajectory via the potentials arising from surface charges σ_j and current distributions \mathbf{h}_j .

3.2 Simulating nanodiscs

In this section our specific particle shape – a nanodisc – will be introduced in a way that is accessible for computer simulations.

3.2.1 The MNPBEM toolbox

The MNPBEM toolbox¹ is a highly versatile framework developed by ULRICH HOHENESTER and ANDREAS TRÜGLER [HT11]. The name stands for “Metallic nanoparticle boundary element method”, and its purpose is to simulate a dielectric environment with embedded bodies with homogenous and isotropic dielectric functions. As is the case for this work, the main application is the simulation of metallic nanoparticles with sharp borders (Fig. 3.3).

The toolbox implements the full solution of Maxwell's equations using a boundary element method (see section 2.2.5) and allows for flexible simulations of the electromagnetic properties of metallic nanoparticles.

Also, electron energy loss spectroscopy (EELS) is implemented [Hoh14] according to equation (3.16).

¹<http://physik.uni-graz.at/~uxh/mnpbem/mnpbem.html>

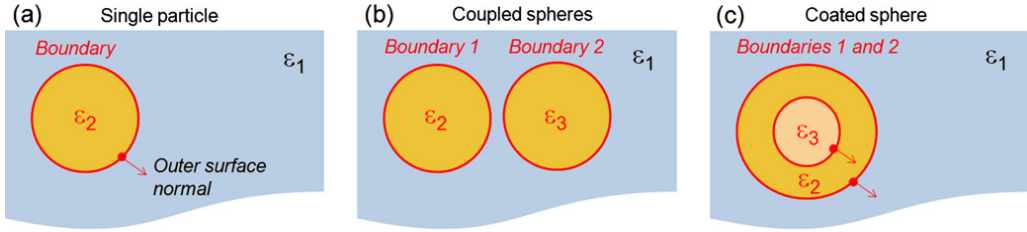


Fig. 3.3: Possible simulations with the MNPBEM toolbox. (a) shows a metallic nanosphere in a dielectric background, (b) are two coupled nanospheres and (c) is a coated one.

Taken from: [HT11]

3.2.2 Structure and discretization

Within the toolbox rather complicated particles such as a “starfish” or particles with rough surfaces can be constructed. A nanodisc however is quite symmetric and to set one up involves three main steps.

First, a regular polygon is built with a certain number of edges. With a large enough number of edges this resembles a circle. Then, the polygon is discretized by dividing the area into surface elements. This can be done quite flexibly, for example areas of interest can be discretized with a larger number of surface elements. This can be very useful because the number of surface elements pushes computer time and memory usage rather rapidly. Finally, the discretized polygon is extruded to a three-dimensional shape and the corners are rounded off (Fig. 3.4).

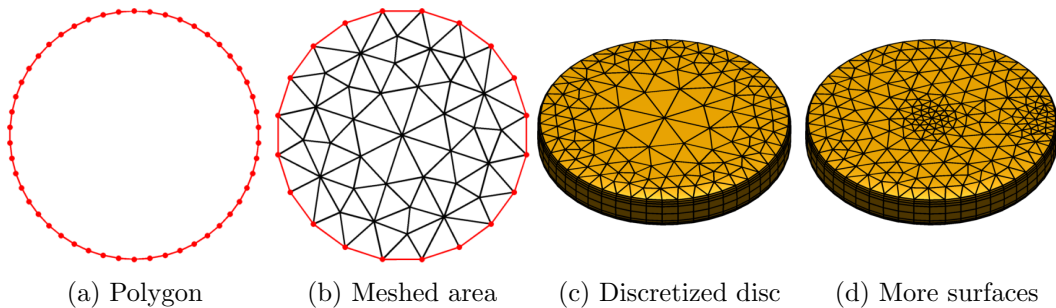


Fig. 3.4: Building a nanodisc within the MNPBEM-toolbox. (a) A polygon approximates a circle, which is (b) discretized with surface elements. This area is (c) extruded to three dimensions. (d) shows the versatility of the discretization routine by having more surface elements at the center and at the edge, used for example if molecules are placed just there.

3.2.3 BEM simulations

Once one or more particles are constructed they can be placed into a dielectric environment and excited with a plane wave or a dipole. The BEM solver processes this input and computes the surface charges and currents (Fig. 3.5). From there it is possible to calculate observables such as the electric field or scattering and absorption cross sections. The BEM solver can use the quasistatic model, solve the full Maxwell equations or perform an eigenmode expansion.

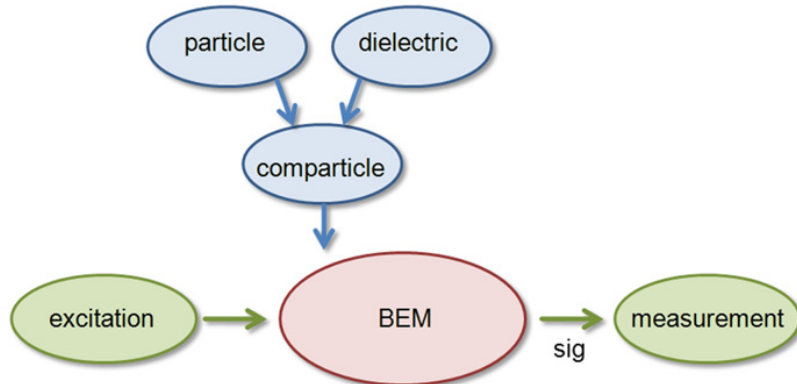


Fig. 3.5: Process of simulating a particle with the MNPBEM toolbox. A particle together with the environment forms a *comparticle* object. This object and an external excitation (plane wave or dipole) communicate with the BEM solver which outputs the surface charges *sig* from which measurements can be carried out.

Taken from: [HT11]

4 Results

4.1 EELS excitation

Let us start our investigation with a representative EELS simulation measurement. We scan the whole probe by varying the impact position of the electron beam and obtain a complete and detailed map of the mode spectrum. It is complete in the sense that “dark” modes can be excited, and indeed the breathing mode couples the strongest to an electron beam hitting a nanodisc at its center. One limitation however is that for modes to interact with an electron beam from above they have to have a perpendicular component that can be excited [note the integral in z -direction in equation (3.16)].

4.1.1 The mode spectrum of a nanodisc

Let us identify the breathing mode in an EELS map. The silver nanodisc is 30 nm thick and 200 nm in diameter (Fig. 4.1). The electron beam’s energy width is 0.2 eV and the refractive index of the surrounding medium is set to 1.25.

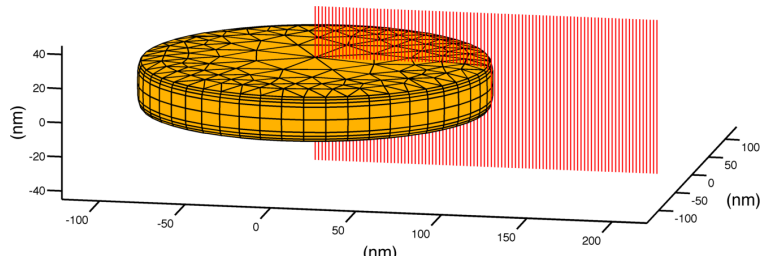


Fig. 4.1: Setup for an EELS simulation where an electron beam (red lines) is sent through or passes by a silver nanodisc.

On the y-axis of Fig. 4.2 we have the impact position of the electron beam ranging from zero, which is the center of the disc, to 200 nm, which is half a diameter away from the disc. The x-axis denotes the *loss energy* in nanometers while the color code gives the *loss probability* in inverse electron volts. This means that the image shows for each distance of the beam from the center the energies that can excite a plasmonic mode and as well the strength of the coupling.

The multipole modes are situated along the edge of the disc, i.e. at 100 nm on the y-axis. The most prominent and broad peak of these edge modes is the dipole (1, 0) at

4 Results

approximately 860 nm followed to the left by the quadrupole (2, 0) at ≈ 560 nm and the hexapole (3, 0) at ≈ 466 nm. Higher orders are further to the left and while the octupole (≈ 426 nm), the decapole (≈ 408 nm) and even the dodecapole (≈ 396 nm) can still be distinguished, the culmination of the rest of them is smeared in this resolution but still displays dominant multipole behavior at about 378 nm.

Similarly, we find the film modes at the center of the disc along the x-axis. The breathing mode (0, 1) at circa 435 nm with its radial symmetry couples very strongly to an electron beam that is sent through the middle of the disc. The second order breathing mode (0, 2) at ≈ 365 nm is still quite clear but higher orders display only very weak peaks. The surface charges for the third order breathing mode (0, 3) at ≈ 345 nm are therefore difficult to plot nicely but still the idea of having only radial symmetry is portrayed.

The double breathing mode (1, 1) can be clearly seen in between film- and edge-modes at ≈ 380 nm but higher orders and mixtures thereof are indistinguishable around ≈ 360 nm.

The rather strong excitation to the very left at 325 nm is the bulk plasmon (Bu). The simulation matches experimental values very well throughout (see [SDH⁺12]).

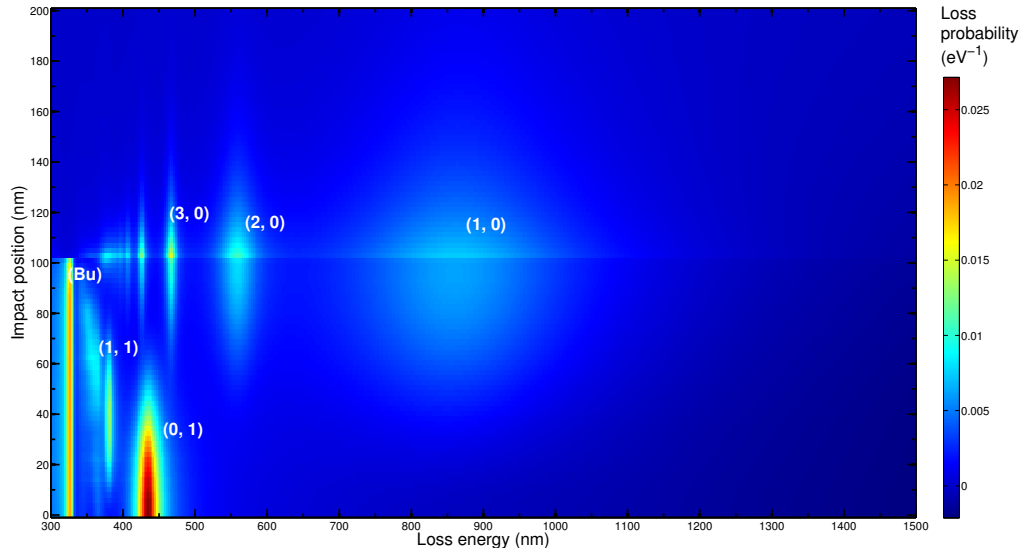


Fig. 4.2: Simulated EELS mode spectrum of a silver nanodisc. At the center of the disc we can see the breathing modes and at the edge the multipolar modes of different order show up. In between lies the hybrid double breathing mode.

4.1.2 Surface charges

So far, the discussion has been an intuitive one deduced from the properties we expect from film respectively surface modes. A handy visual way to confirm that the

established peak at 435 nm is indeed the breathing mode (0, 1) is plotting the surface charge distribution. For this we send an electron beam through the center of the disc and compute the surface charges on the particle for the corresponding loss energy.

The result is shown in Fig. 4.3. Positive charges around the center of the disc are separated by a neutral azimuthal node line from negative charges. This is the breathing mode. The oscillations are analogous to an acoustic wave from a drum being hit in the middle.

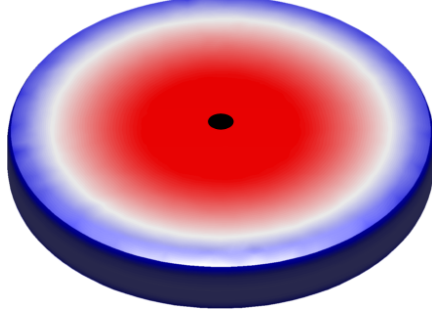


Fig. 4.3: Surface charges for a 200×30 nm silver nanodisc that was excited by an electron beam (black dot). Positive charges (red) originate from the center and are separated from negative charges (blue) by a neutral ring (white). These are the characteristics of the breathing mode at 435 nm.

All other modes respectively peaks mentioned in section 4.1.1 are shown in Fig. 4.4. The first two lines are the surface charges for the multipole modes from dipole to dodecapole; the third line is the second and third order breathing modes as well as the hybrid double breathing mode. The fourth line displays the smeared culminations for both multipole and breathing modes and the bulk plasmon.

All surface charge plots take the imaginary part of the total surface charges inside the particle. The real part is equally suited for an investigation but drops at the resonance frequency; this is a phase shift problem. The imaginary part readily shows the response of the metallic nanoparticle at the resonance frequency.

Regarding the position of the impact beam, it was chosen central for breathing modes and almost at the edge for edge modes (at 90 nm for a radius of 100 nm). The hybrid mode and the bulk were excited in the middle at 50 nm. For comparison, Fig. 4.5 shows the surface charges for attempts to excite the film breathing mode at the edge and vice versa for the dipole mode at the center. In short, it does not work.

4 Results

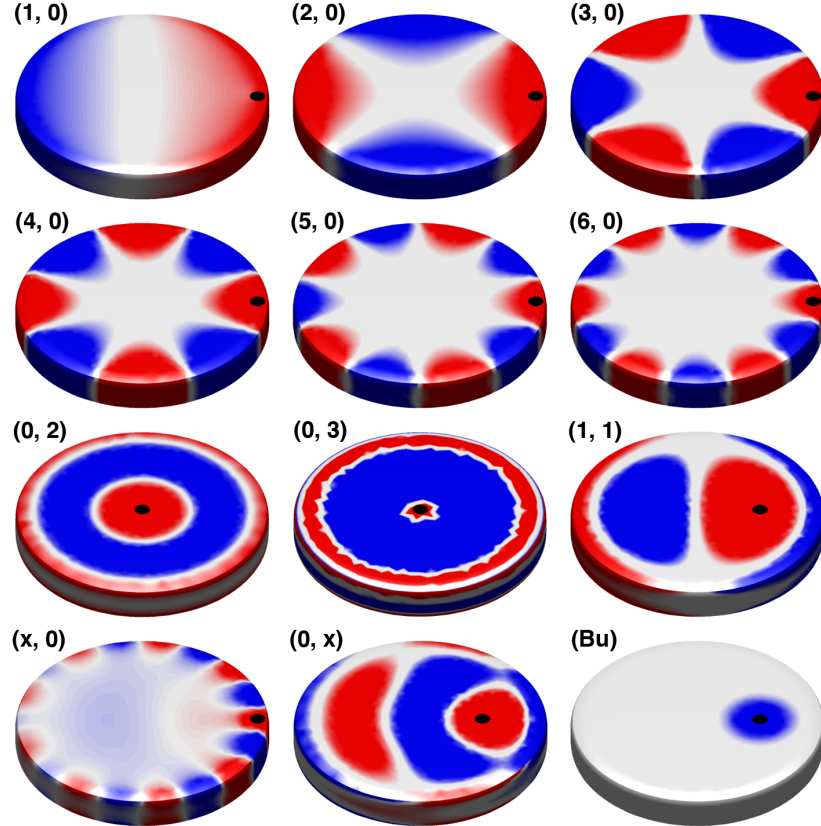


Fig. 4.4: Simulated total surface charges inside the particle for an electron beam excitation at positions indicated by black dots. The captions are the number of radial and azimuthal node lines ($\#R, \#A$) starting with the dipole (1, 0), the quadrupole (2, 0), the hexapole (3, 0), the octupole (4, 0), the decapole (5, 0) and the dodecapole (6, 0). (0, 2) is the second order breathing mode with two azimuthal node lines; (0, 3) approximates the third order which is hard to distinguish. (1, 1) shows the hybrid double breathing mode with both radial and azimuthal node lines. ($x, 0$) is the plot for the smeared culmination of all higher order multipole modes and ($0, x$) is the same for higher order breathing and hybrid modes. (Bu) is the bulk plasmon which is mainly dependent on the particle geometry and responds at the position of the impact beam.

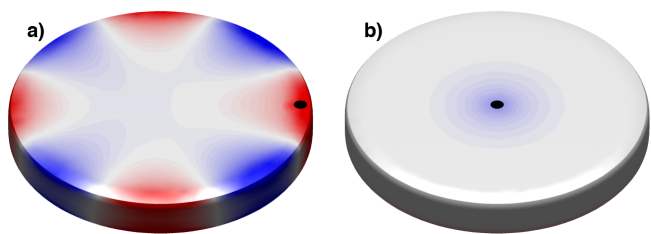


Fig. 4.5: Failed attempts to a) excite the breathing mode at the edge of the disc and b) excite the dipole at the center. As can be seen in Fig. 4.2 the breathing mode overlaps with the octupole (at different positions on the particle) for this disc geometry and the response shows just that – a slightly deformed octupole. The dipole has no other modes nearby and cannot be excited resulting in only a small response to the electron beam.

4 Results

4.2 Plane wave excitation

We now turn to the excitation of plasmons with a plane wave, i.e. light. From the discussion in section 3.1.1 we expect that for straight impact of the light the dipole mode will be visible, while for the observation of other modes with no dipole moment we need to tilt the light source.

4.2.1 Straight impact

For now, the geometry of the disc stays the same at $200\text{ nm} \times 30\text{ nm}$. The result is shown in Fig. 4.6 where for each wavelength of the incident light the scattering cross section is calculated as a measurement of resonant behavior. The insets are plots for the surface charges at a given peak as well as the disc with direction and polarization of the light wave.

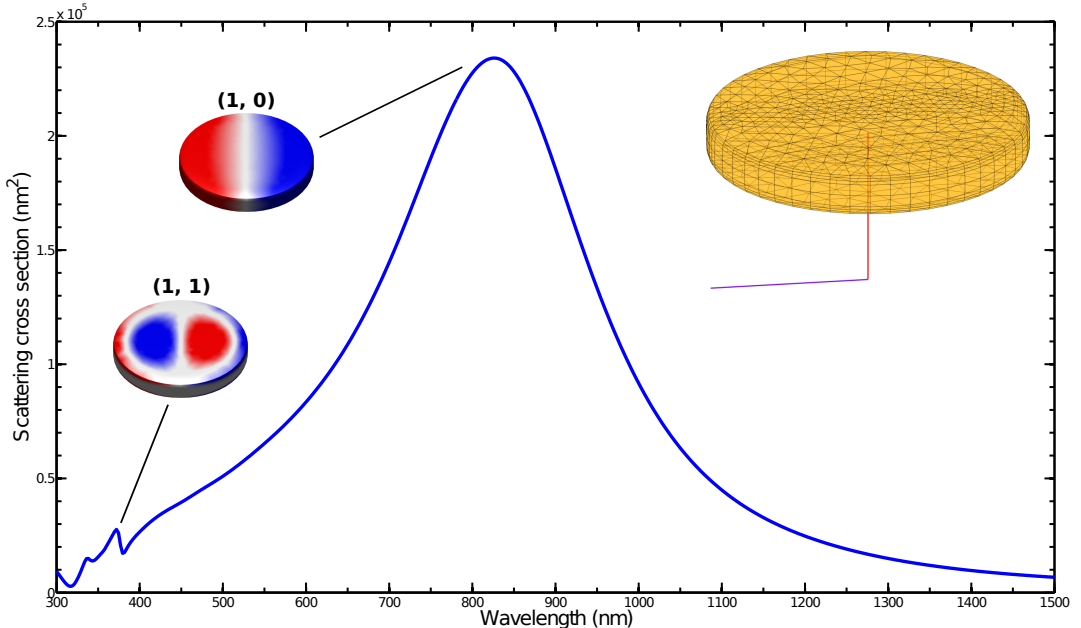


Fig. 4.6: Scattering cross section for a silver nanodisc which is excited with a plane wave that hits the particle straight on (red line in inset). The purple line in the inset shows the direction of the magnetic field (polarization). Surface charges are added for the two clearly visible peaks, namely the dipole mode $(1, 0)$ and the double breathing mode $(1, 1)$. Disc size is $200\text{ nm} \times 30\text{ nm}$, refractive index of the medium is 1.25.

As expected, the dipole $(1, 0)$ is dominant at $\approx 827\text{ nm}$. At $\approx 371\text{ nm}$ the double breathing mode $(1, 1)$, which possesses a dipole moment too, lights up.

4.2.2 Tilted impact

Without further ado, Fig. 4.7 shows the results for light at an oblique angle of 45° .

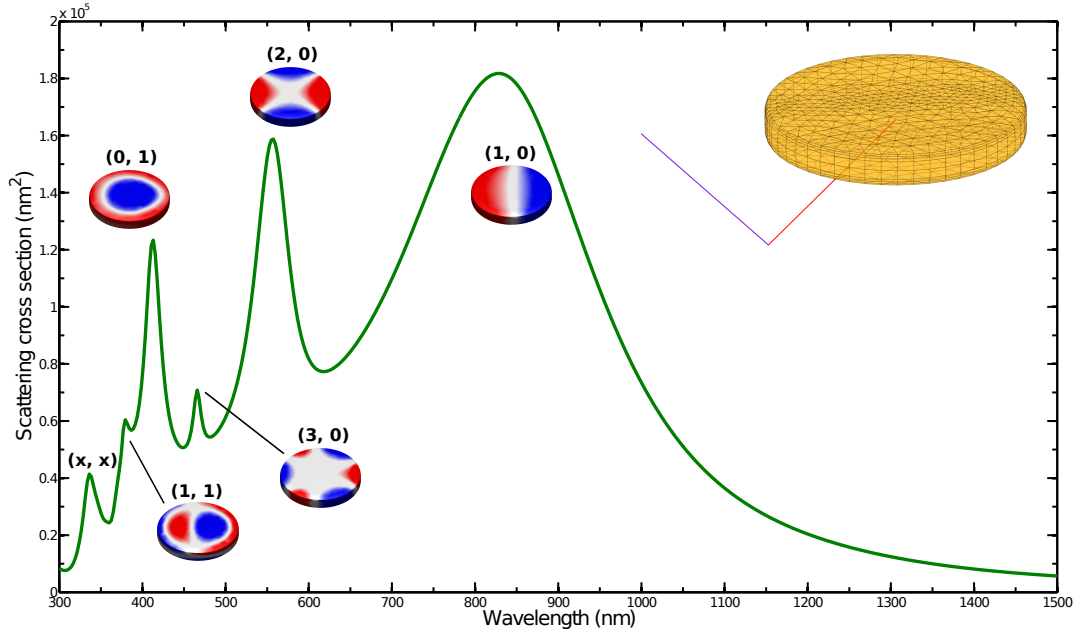


Fig. 4.7: Scattering cross section for oblique light at 45° (red line in inset) and p-polarization (purple line). The small insets show the calculated surface charges for dipole, quadrupole, hexapole, breathing mode and double breathing mode. The leftmost peak (x, x) is an undefined accumulation of higher order modes. Disc size is $200\text{ nm} \times 30\text{ nm}$, refractive index of the medium is 1.25.

As was the case for straight impact, the dipole mode lies at about 829 nm and the double breathing mode at 379 nm, respectively. But now we can also see the quadrupole at 557 nm, the hexapole at 466 nm and, most importantly, the breathing mode at 413 nm. This is a crucial result. All expected modes show up in the spectrum.

Keeping Fig. 3.1 in mind we can reason that the more of a wavelength we are able to fit into the nanodisc the stronger modes with no net dipole moment should be able to couple. This is confirmed for the three angles 30° , 45° and 75° from the z-axis in Fig. 4.8. For 30° , the breathing mode $(0, 1)$ is visible very well, but the double breathing mode $(1, 1)$ and the hexapole $(3, 0)$ manifest only in small peaks. For 75° the breathing mode is indeed pushed to be the dominant peak shadowing other modes under investigation. However, at a slightly higher wavelength than the breathing mode the octupole $(4, 0)$ begins to be visible. A medium oblique angle of 45° results in the smooth graph that was looked at in more detail in Fig. 4.7.

4 Results

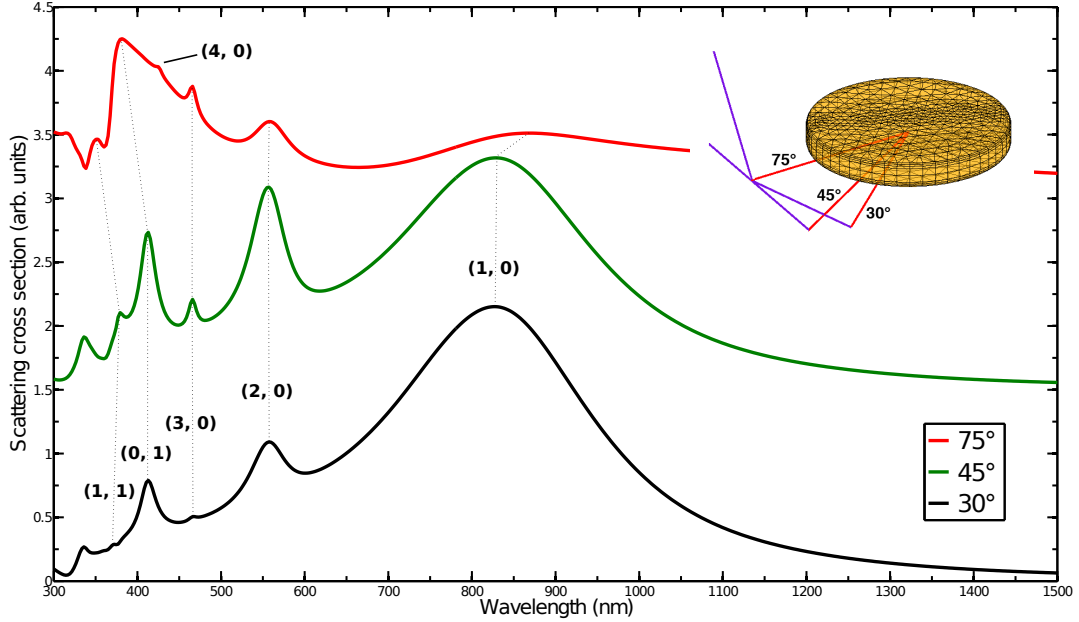


Fig. 4.8: Dependence of the scattering cross section of (particularly non-dipole) modes on the angle of the incoming light (red lines in inset) from the z -axis. The plots for 30° (black), 45° (green) and 75° are offset for better readability. The purple lines in the inset are the directions of the B -field (polarization). Disc size is 200 nm \times 30 nm, refractive index of medium is 1.25.

4.2.3 Dependence on disc size

It is well known that the resonance behavior of nanoparticles can be tuned by changing their shape (see e.g. [BTJ⁺10] and references therein). The colors of church windows are an example of how differently shaped metallic nanoparticles result in a vast variety of resonant wavelengths. For this effect the absolute size of the particles does not matter that much – the important factor is the aspect ratio of their axes.

The Fröhlich condition 2.76 can be generalized to contain geometrical factors L_1 , L_2 and L_3 :

$$\Re \{\varepsilon(\omega)\} = \left(1 - \frac{1}{L_i}\right) \varepsilon_m. \quad (4.1)$$

For a sphere, $L_i = 1/3$ [BH83, p. 146]. For flattened spheres, the geometrical factors L_i are smaller resulting in a smaller resonant dielectric function $\varepsilon(\omega)$ and thus a smaller resonant frequency ω (cf. equation 2.31). At least in this sense strongly flattened spheres can approximate disc shapes.

Fig. 4.9 shows the scattering cross section for a disc that is flattened from 100 nm \times 30 nm to 300 nm \times 30 nm.

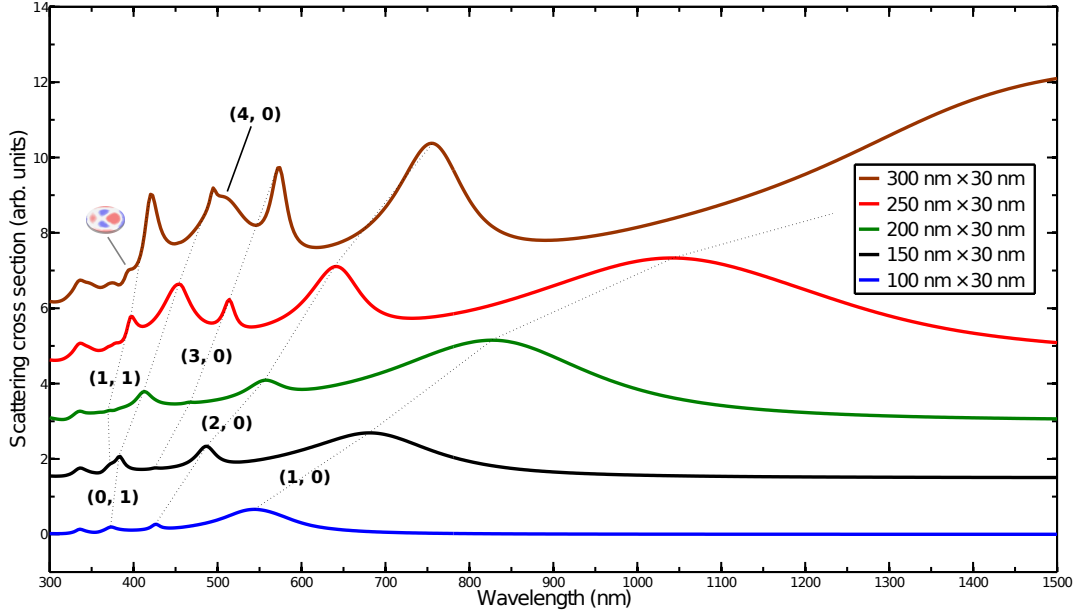


Fig. 4.9: Scattering cross sections for different disc sizes (offset for readability). The modes are redshifted due to the flattening of the particle, the breathing modes become more distinguished because of retardation effects in bigger particles. For a diameter of 300 nm (brown line) the octupole (4, 0) starts to show. Peaks at larger energies than the double breathing mode (1, 1) are a culmination of higher orders and hybrid modes (surface charges for one of them in small semitransparent inset). Angle is 45° , index is 1.25.

Like with more or less tilted light, the breathing modes become more distinct the more of a retardation effect we bring into play – this time by increasing the disc's diameter. While the thickness stays at 30 nm, the diameter is changed from 100 nm to 150 nm, 200 nm, 250 nm and finally 300 nm. At 300 nm the octupole (4, 0) becomes visible for plane light at about 507 nm.

The spectrum is stretched by the dipole wandering off to lower energies. This redshift is intuitively explained by a weaker restoring force, i.e. a longer resonant wavelength, for a smaller distance between the bottom and the top of the disc compared to the exciting wavelength (cf. Fig. 3.1).

4.2.4 Polarization dependence

The mode spectrum depends on the polarization of the incident light wave. Viewing the nanodisc from the side the two options that comply with Maxwell's theory are a magnetic field that points into the direction of the viewer (s-polarization) and a magnetic field that points in a direction perpendicular to both the s-polarization vector and the propagation direction (p-polarization). Both polarizations are simulated

4 Results

and shown in Fig. 4.10.

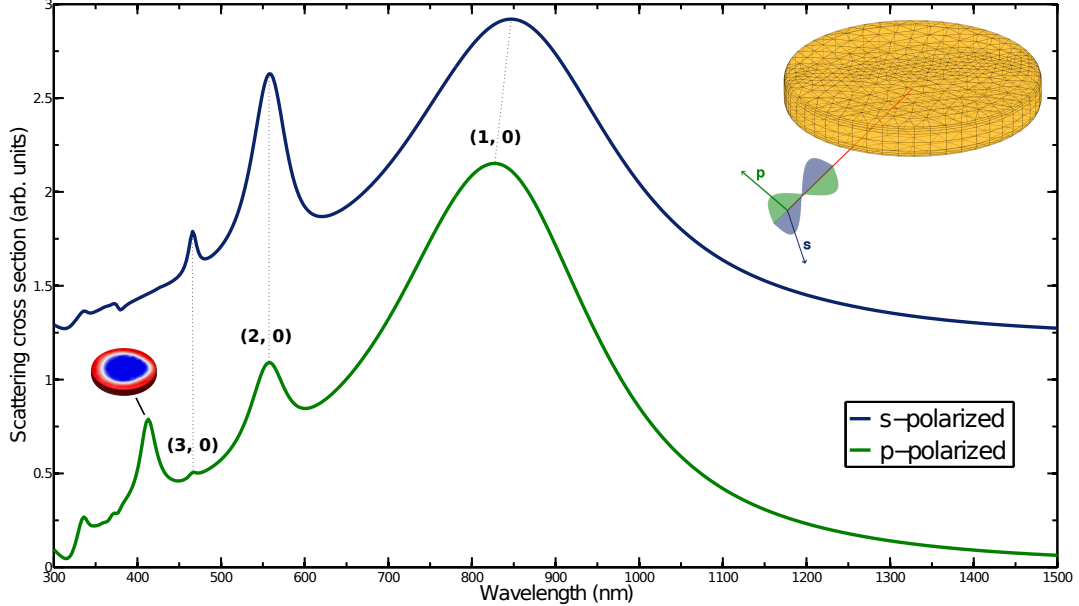


Fig. 4.10: Polarization dependence of the scattering cross section (offset for readability). While the multipole modes are visible for both p-polarization (green in graph and green B -field in inset) and s-polarization (dark blue in graph and inset) the breathing mode (small inset) is only visible for p-polarized light. The angle of the incoming wave is 45° (red line in inset). Disc size is $200 \text{ nm} \times 30 \text{ nm}$, index is 1.25.

We noted in section 2.4.1 that we need to use p-polarized light to access the full spectrum which is reproduced in the fully retarded computer simulation. The dipole redshifts slightly while the quadrupole and the hexapole stay at the same wavelengths although the latter is quite a bit weaker for p-polarization. But, most importantly, the breathing mode is invisible for s-polarization and a clear peak for p-polarized light.

4.2.5 Dependence on the index of the surrounding medium

Together with the aspect ratio the surrounding dielectric medium is the most important factor that determines the position of the mode peaks. Very small changes in the environment can shift the modes considerably [PJPSLMM05]. This must potentially be given thought for sensing applications, for example when an immersed probe in water is excited with a laser. The laser can heat up the water and change its refractive index enough to result in peak-shifts of several nanometers.

Until now, the refractive index of the medium was set to 1.25. The reason for this is that accompanying experiments use a glass substrate with an index of 1.46 (quartz

glass). The approximate mean value of air ($n = 1$) and glass is meant to substitute for missing substrate effects.

Fig. 4.11 shows the simulated results for three different refractive indices. Since the discrepancies are quite big, the modes shift very notably.

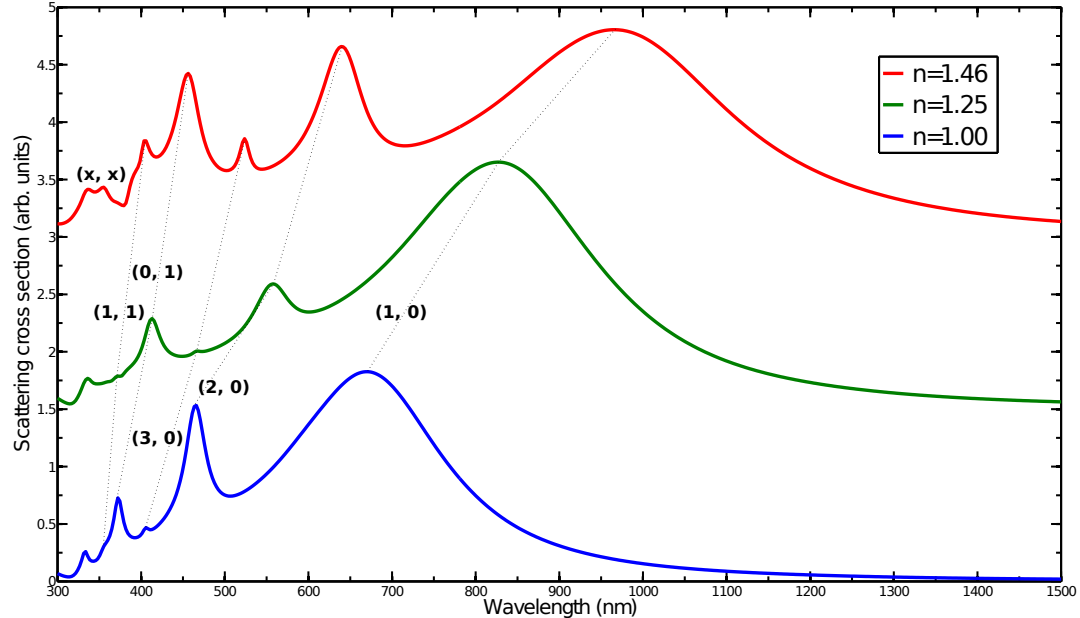


Fig. 4.11: Scattering cross section for nanodiscs surrounded by media with different refractive indices. The indices are 1.0 for air/vacuum (blue line), 1.46 for quartz glass (red line) and 1.25 for an approximate mean value (green line). All modes are shifted to longer wavelengths and more distinct for higher indices. The angle of the incident wave is 45° , the disc size is $200 \text{ nm} \times 30 \text{ nm}$.

All modes are redshifted for higher indices with the dipole experiencing the biggest change. This stretches the spectrum and some modes like the hexapole and the double breathing mode benefit from this in the sense that they are a lot better to distinguish.

4.2.6 Comparison between silver and gold

We have stated in section 2.2.7 that silver should be a better choice for studying the breathing modes due to interferences of the d-band structure when using gold. Fig. 4.12 shows that this is indeed the case – only modes above $\approx 620 \text{ nm}$ (namely the dipole and the quadrupole) are visible on the golden nanodisc.

4 Results

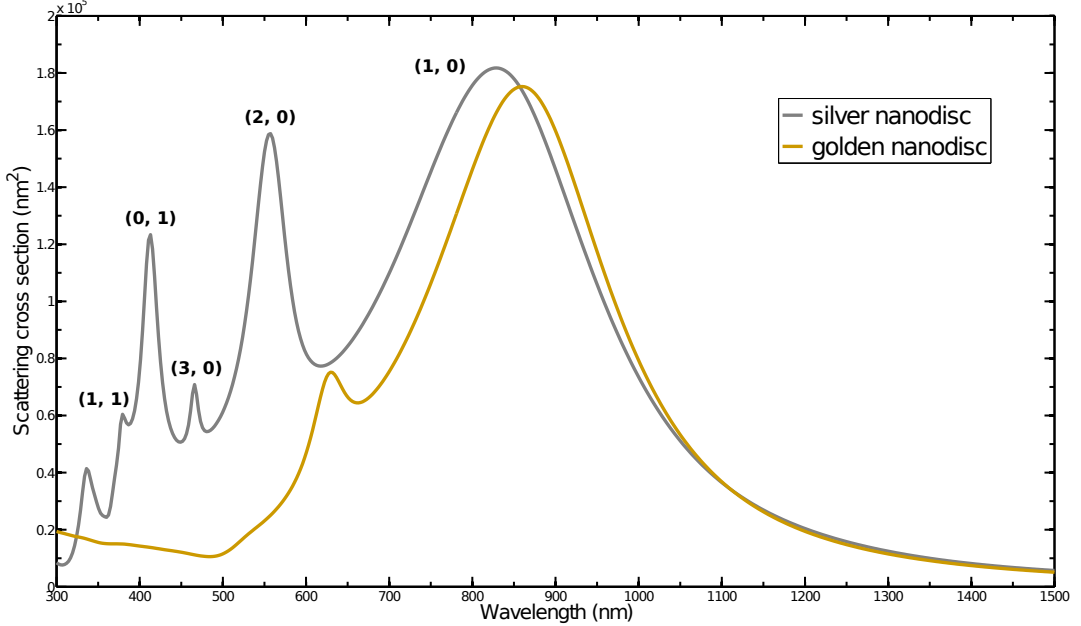


Fig. 4.12: Scattering cross sections for a silver and a golden nanodisc. Gold is not suitable for studying the breathing modes because they are shielded by the d-band structure. Angle is 45° , disc size is $200\text{ nm} \times 30\text{ nm}$, the index is set to 1.25.

4.2.7 Experimental results

After proposing that the breathing mode $(0, 1)$ should be visible for tilted light the idea was pursued by our experimental nano optics group. The measurements, especially for single nanodiscs, proved to be challenging, but after a working setup had been achieved the breathing mode could optically be seen clearly. For an in-depth look we refer to the results compiled in [Kru14] and only briefly note that the experiments match the simulations very well throughout regarding different oblique angles for the incoming light wave, different polarizations, varying disc diameters and the positions of the modes. Also, different dispersion relations of multipole and breathing modes were measured underlining their fundamentally different nature.

4.3 Dipole excitation

We now turn our interest to a third kind of excitation – the excitation of silver nanodiscs via oscillating dipoles that are placed in its vicinity. This is an important concept for plasmonic sensing applications. The dipole acts on the nanoparticle by changing the dielectric surrounding and strongly modifies its mode spectrum. The dipole can use the nanodisc as an “antenna” and enhance the emission strength by

magnitudes. The breathing mode could prove useful to such applications because of its relative strength and sharpness when tuned properly (cf. Sec. 4.2.5).

Experimentally, one obtains *quantum dots* that emit over a range of frequencies defined by their structure. To couple such quantum dots possessing a fixed wavelength with a nanoparticle we could use our freedom of choice for the aspect ratio of the particle and the index of the dielectric to shift the desired modes to an appropriate wavelength. In our computer simulations however we have the ways to choose the wavelength the dipole emits arbitrarily and keep the disc size constant and consistent with our investigation so far.

4.3.1 Coupling of dipoles to dark modes

Let us again check the full mode spectrum. This is done by placing dipoles close to the nanodisc and running through emission energies. The molecules hover 10 nm above the disc and are placed at the edge, the center and the middle. To determine resonant behavior we use the molecules' decay rate.

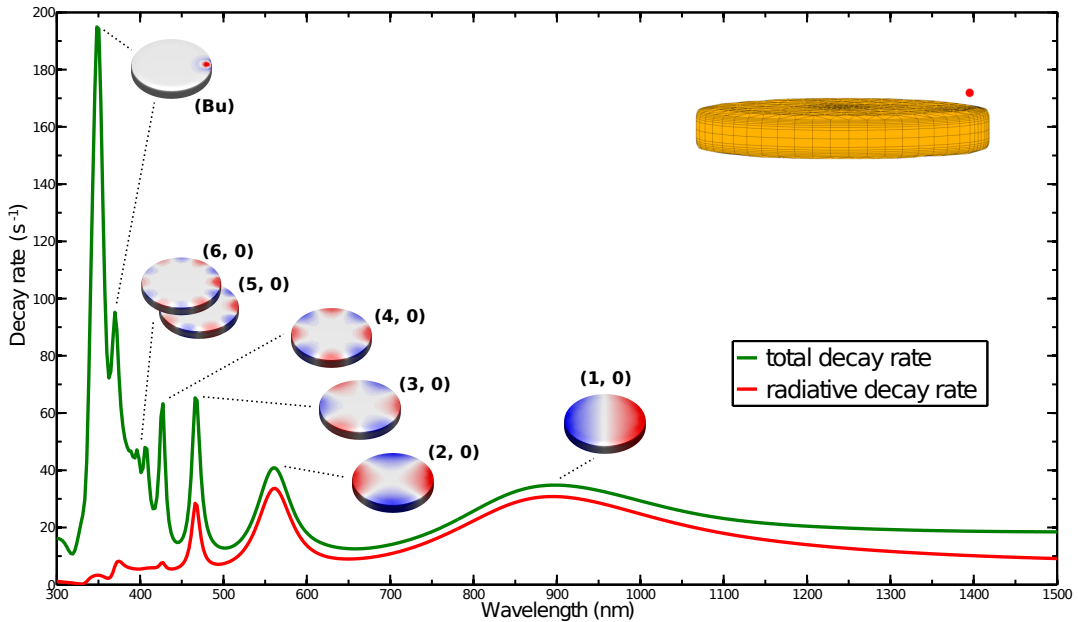


Fig. 4.13: Total (green line) and radiative decay rate (red line) of a molecule/dipole placed close to the edge of a nanodisc. All multipole modes show up (calculated surface charges in insets) and radiate to the far field. Since the dipole can excite arbitrary modes, higher orders culminate with the bulk to the strong leftmost peak labelled *(Bu)*. Silver disc size is 200 nm × 30 nm, the index is set to 1.25.

There are no surprises and the spectrum is analogous to the one obtained with EELS excitation. The dipole can excite all modes.

4 Results

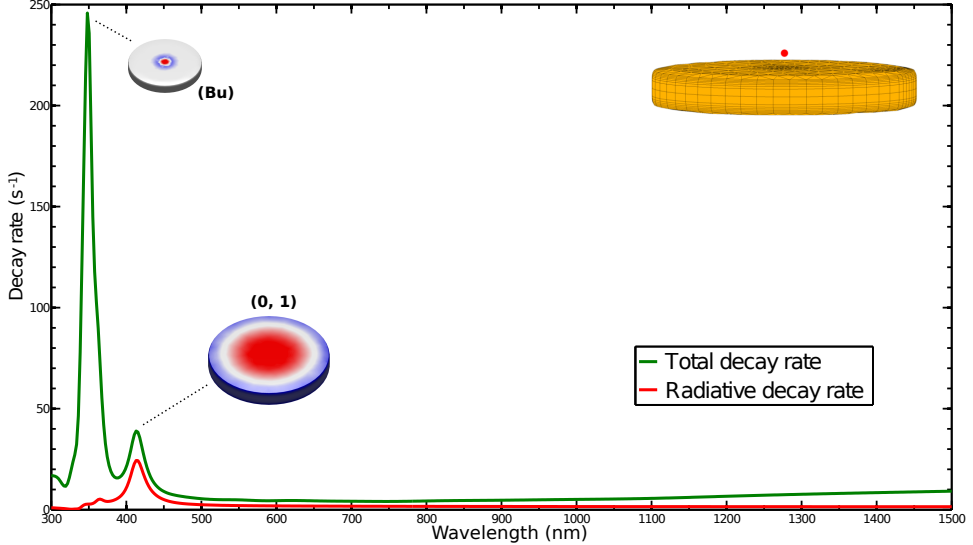


Fig. 4.14: Total (green line) and radiative decay rate (red line) of a molecule/dipole that hovers 10 nm above the center of a silver nanodisc (inset). The breathing mode (surface charge in inset) shows up clearly for total and radiative decay. The strong bulk gives the material response of the disc to the oscillating dipole.

In Fig. 4.13 the decay rate is plotted when the molecule is placed at the edge (90 nm for a radius of 100 nm) of the disc. The edge modes are visible very well. In detail, the dipole lies at ≈ 895 nm, the quadrupole at ≈ 560 nm, the hexapole at ≈ 466 nm, the octupole at ≈ 427 nm, the decapole at ≈ 406 nm and the dodecapole at ≈ 396 nm. There is even a small spike for the multipole (7, 0) at ≈ 389 nm. Higher orders are overlapping with the very strong bulk. Furthermore, the multipole modes exhibit radiative decay (albeit decreasing strongly for higher modes) and are therefore detectable in the far field.

Fig. 4.14 shows the same simulation when the molecule is placed above the center of the disc. Apart from the strong bulk that shows the response of the disc to the dipole directly only the breathing mode is visible at ≈ 413 nm and also radiates to the far field.

For Fig. 4.15 the dipole was put at 50 nm, that is at half a radius from the center. Although weaker, the breathing mode and the multipoles are visible. Plus, the hybrid double breathing mode becomes excited at ≈ 377 nm and transports energy both radiatively and non-radiatively.

Lastly, Fig. 4.16 neglects the total decay rate and gives an overview of the radiating modes.

Again, we can see that both edge and film modes emit radiatively. Note how the multipole modes overlap with the breathing modes in the middle, which is why here

4.3 Dipole excitation

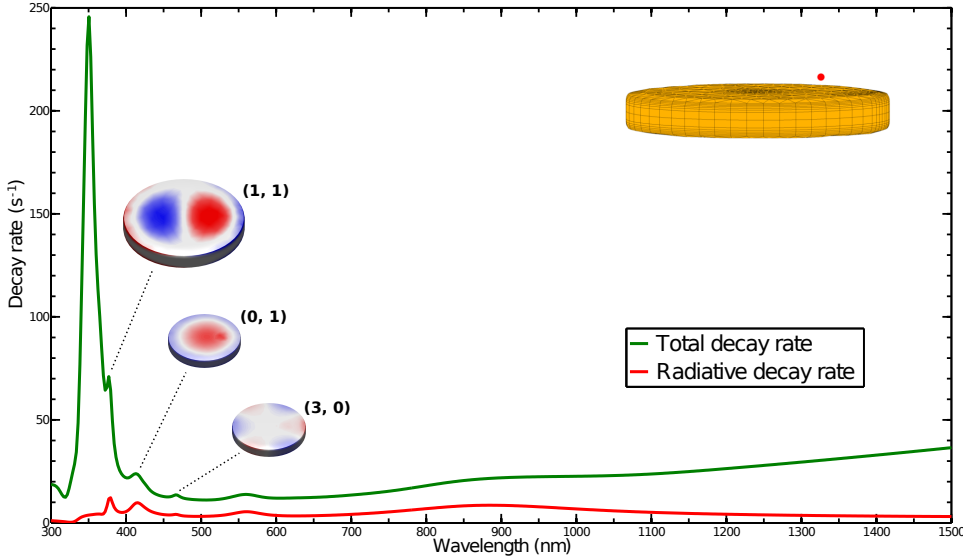


Fig. 4.15: Decay rates of a molecule above the middle of the disc. In between edge and film modes lies the hybrid double breathing mode $(1, 1)$ that becomes visible close to the bulk.

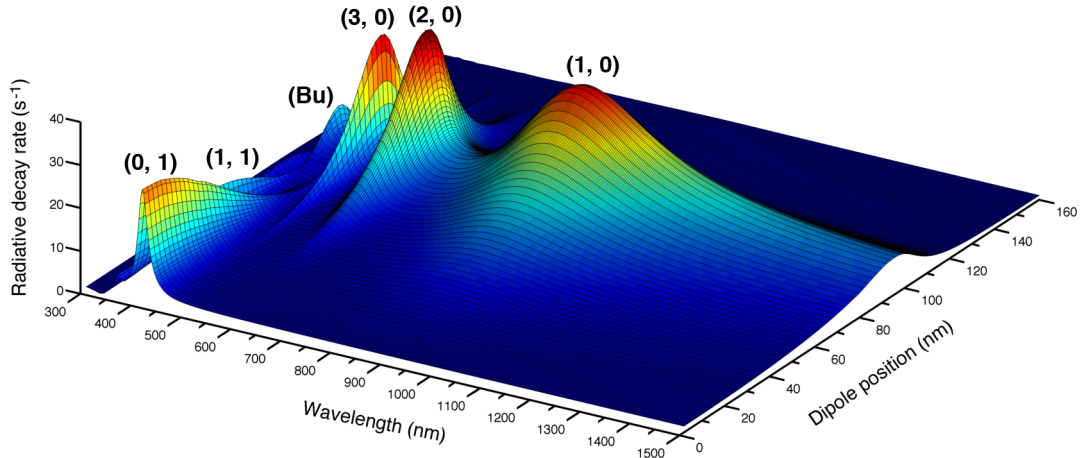


Fig. 4.16: Radiative decay rate as a function of the wavelength and the distance of the dipoles from the center of the disc. Edge, breathing and hybrid modes emit radiatively; edge and film modes overlap in the middle but not at the center or the edge of the disc. Disc size is $200 \text{ nm} \times 30 \text{ nm}$, index is 1.25.

all modes can be excited (cf. Fig. 4.15). However, the breathing mode does not reach the edge and the multipole modes do not reach the center. This is why at the edge we only see edge modes (cf. Fig. 4.13) and vice versa (cf. Fig. 4.14).

4 Results

4.3.2 Dependence on the dipoles' orientation

Thus far the dipoles were oriented along the z-axis. Penetrating the disc this way, the dipole's field varies the most and is therefore the least confined to symmetry restrictions. Just one simulation is picked but this was constantly observed and holds true for all others. Some peaks are shifted for other orientations. For a quick check, three alignments along Cartesian coordinates are simulated in Fig. 4.17. The setup is the same as for Fig. 4.13 (dipoles over the edge of the disc).

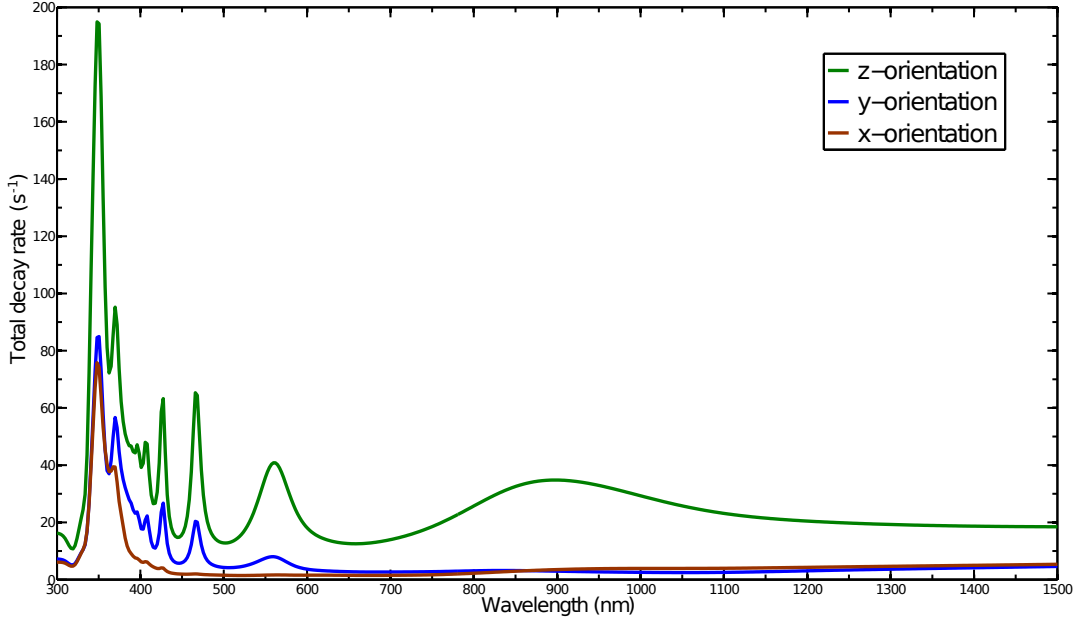


Fig. 4.17: Total decay rate for dipoles situated 10 nm above the edge of the disc. The dipoles are oriented differently, namely in x-direction (brown line), y-direction (blue line) and z-direction (green line). Disc size 200 nm \times 30 nm, index 1.25.

The dipole that is oriented along the z-axis results in the clearest peaks and highest decay rates.

4.3.3 Quantum yield

We are interested in how much of the energy is dissipated non-radiatively and how much is transported to the far field. The quantum yield is the ratio of those two channels (see section 2.3.3).

To calculate this, we set up a nanodisc and place dipoles along the x-axis (Fig. 4.18).

Then, the emitting wavelength is varied within the usual range and we calculate for each dipole position and each wavelength the quantum yield; the results are shown in Fig. 4.19.



Fig. 4.18: Silver nanodisc with dipoles in its vicinity. The dipoles are placed in x-direction, starting from the center to one radius (here 100 nm) outside of the disc.

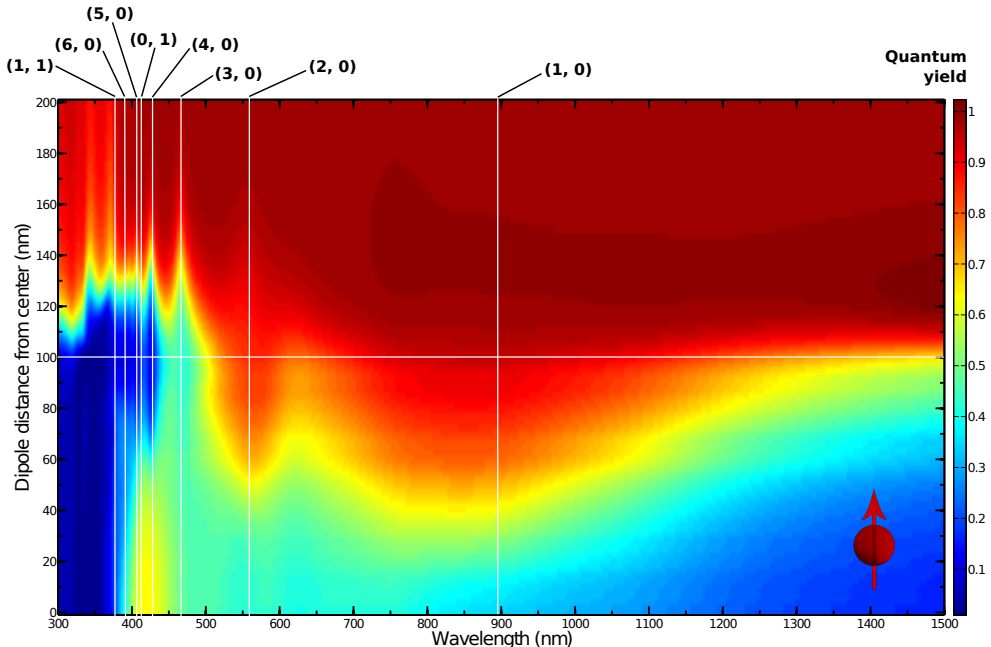


Fig. 4.19: Quantum yield for dipoles that are oriented along the z-axis and situated along the x-axis. The horizontal white line marks the edge of the disc, the vertical white lines are positions of resonant modes. Disc size 200 nm \times 30 nm, index 1.25.

We need to keep in mind that red areas in Fig. 4.19 show a high ratio of radiative to total decay – this does not mean that the decay rate is high in absolute numbers. Dipoles at some distance to the nanodisc (the white horizontal line is at the edge of the disc) cannot couple to the disc anymore and decay radiatively like in free space. At the center of the disc the dipoles can use the breathing mode – vertical white line labelled $(0, 1)$ – as a radiative decay channel. In between the center and the edge of the disc the molecules can decay radiatively through the dipole and the quadrupole mode. However, higher order modes do not seem suitable to enhance the quantum yield as strongly. For the hexapole, the quantum yield is only about half the value of that for the dipole mode at the edge. Modes with more than six poles do not show

4 Results

enhanced radiative decay throughout the disc but only in a small area about 30 nm out.

Fig. 4.20 shows the same data extracted at four wavelengths corresponding to the quadrupole, hexapole, the breathing and the double breathing mode.

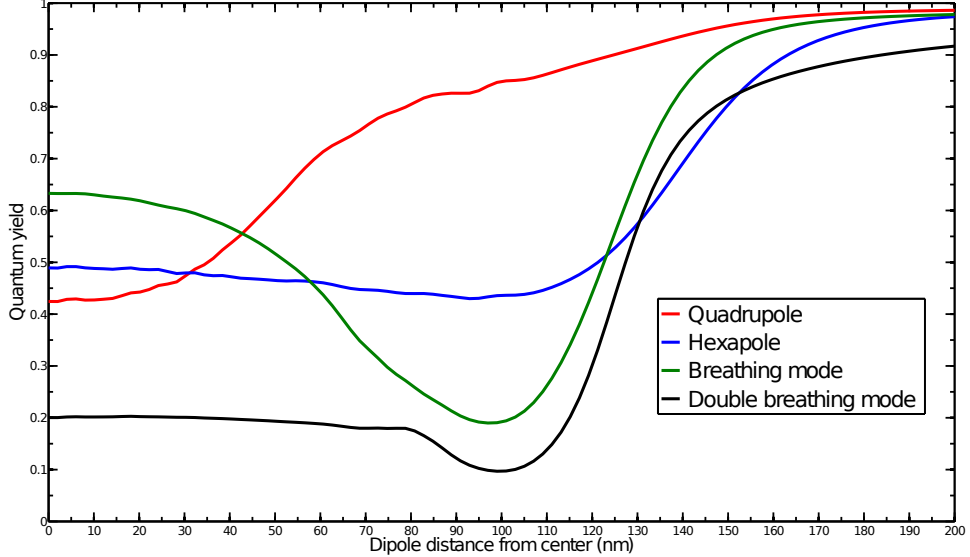


Fig. 4.20: Quantum yield for different modes as a function of the dipole distance from the disc center. Disc size 200 nm × 30 nm, index 1.25.

The molecule excited with the energy of the breathing mode has a quantum yield around 0.6 in the middle which then decreases monotonously until the dipoles are too far away to couple to the disc anymore. For the quadrupole the disc has its lowest quantum yield at the center and it increases monotonously to the edge. At the hexapole the quantum yield is more or less constant throughout the disc, as is at the double breathing mode but with a notable decrease around the edge.

Since we are not looking at absolute values we cannot easily say that dipoles in z-orientation will always have the greatest quantum yield. Thus, Fig. 4.21 shows the quantum yield for x- and y-orientation as well as the difference between z- and x- resp. y-direction.

A first visual comparison between the quantum yield for z-oriented dipoles (Fig. 4.19), x-oriented dipoles (Fig. 4.21a) and y-oriented dipoles (Fig. 4.21c) suggests that because of the highest absolute radiation for z-orientation the quantum yield is as well largest in this case. The red areas for z-orientation cover the red areas for x- and y-orientation. Contrary to this, actually calculating the difference (Fig. 4.21b and Fig. 4.21d) reveals quite a bit of discrepancy. However, areas of higher quantum yield for x- and y-orientation (blue areas) are focussed mainly around the bulk. The small peak-shifts for different orientations also play a role.

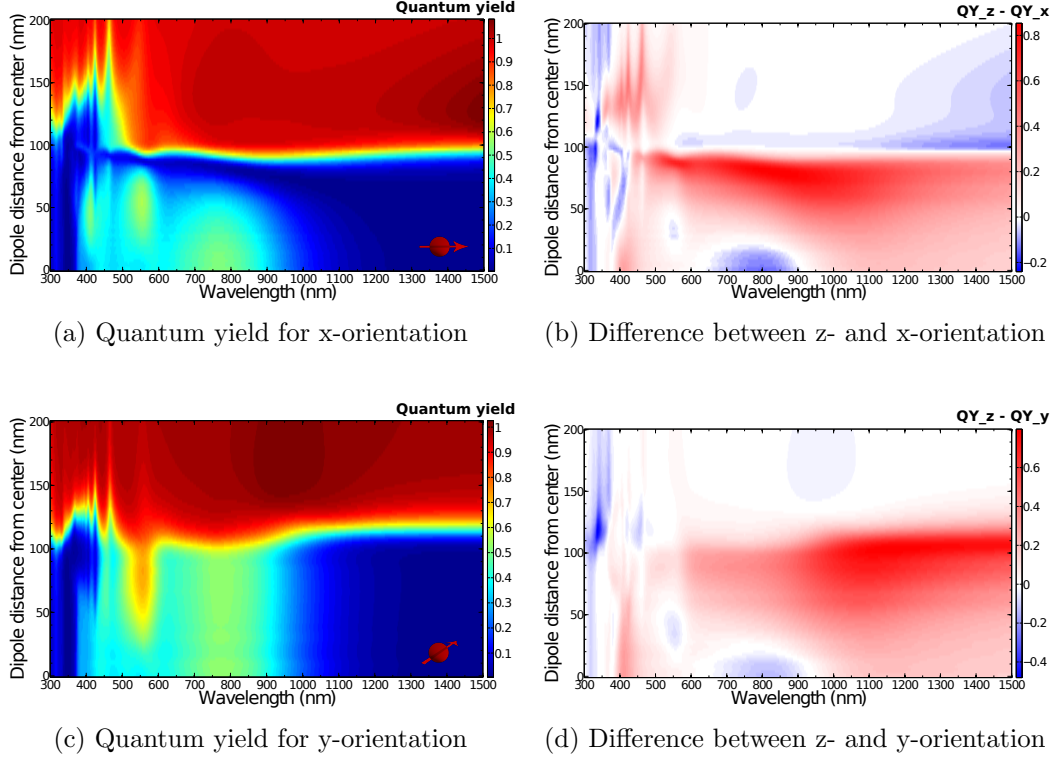


Fig. 4.21: Quantum yield for dipoles oriented along (a) x and (c) y, as well as the difference to z-orientation. Blue areas in (b) and (d) mark a higher quantum yield than for z-orientation. The main difference is around the bulk.

4.4 Förster type energy transfer

An emitter is put above a silver nanodisc and acceptors are scattered across the plane. We calculate the enhancement of the energy transfer rate in presence of the nanoparticle. We remember equation (2.60) to be the scaling function of interest:

$$T(\omega_0) = 16\pi^2 k^2 R^6 |\hat{\mathbf{n}}_A \cdot G(\mathbf{r}_A, \mathbf{r}_D) \hat{\mathbf{n}}_D|^2. \quad (2.60)$$

The absolute value that is being squared in equation (2.60) is calculated via Green's function and multiplied with the orientation of the accepting dipole. This is done for both the total field in presence of a nanodisc and the dipole field in free space; the difference is plotted for various energies of the emitter and orientations of the acceptors.

4.4.1 Energy transfer in free space

Fig. 4.22 shows the setup for the simulation, however, for now in absence of the nanodisc. The donor points upwards and is placed at the center. It emits at the energy corresponding to the breathing mode. The acceptors are scattered across the

4 Results

plane and they too are oriented along z. The color code is the value of $T(\omega)$ that scales the energy transfer. It has the rather abstract dimension $[T(\omega)] = \text{rad}^4$.

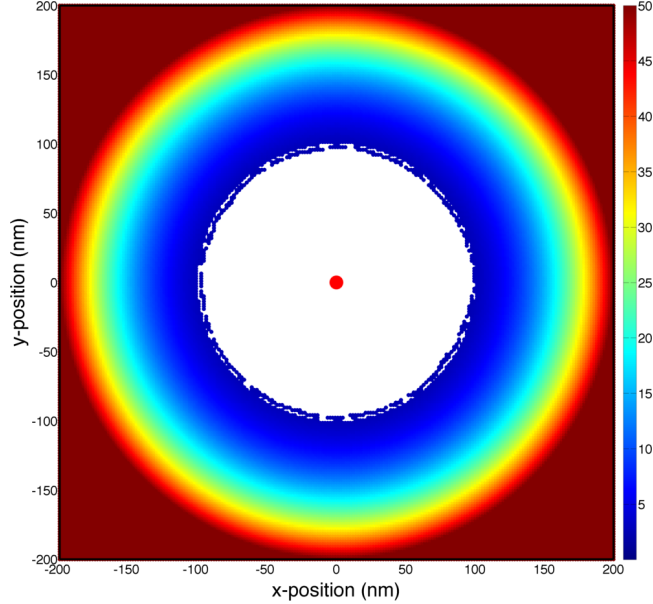


Fig. 4.22: $T(\omega)$ as the scaling function for the energy transfer in free space. The high values represented by red areas are merely the R^6 dependence. Disc size 200 nm \times 30 nm, index 1.25.

It is stressed that what we can see is merely the R^6 dependence of $T(\omega)$ and the red areas do not necessarily show an efficient energy transfer. In this sense, monotonous radial increase of $T(\omega)$ should not be interpreted as a physical connection to the energy transfer. What we are interested in instead are fluctuations along an azimuthal line around the donor. In this case, with no nanoparticle present, there are none. Every acceptor at a certain distance from the emitter feels the same weak dipole field. This changes when we bring a metallic nanoparticle into play in the next section.

4.4.2 Energy transfer in presence of nanodisc

We now calculate $T(\omega)$ for the energy transfer between a donor that is put 10 nm above a silver nanodisc and an array of acceptors. They too have a distance of 10 nm to the surface of the disc. Their orientation is varied to both coincide with the donor's orientation and alignments perpendicular to that. Fig. 4.23 to Fig. 4.28 show the results for the multipole modes dipole, quadrupole and hexapole and for the breathing mode, the double breathing mode and the bulk.

Fig. 4.23 shows $T(\omega)$ for dipole excitation. In the first row each subplot is scaled individually to highlight the features and the areas of more efficient energy transfer. What we can see is that when the donor's orientation matches the acceptors

4.4 Förster type energy transfer

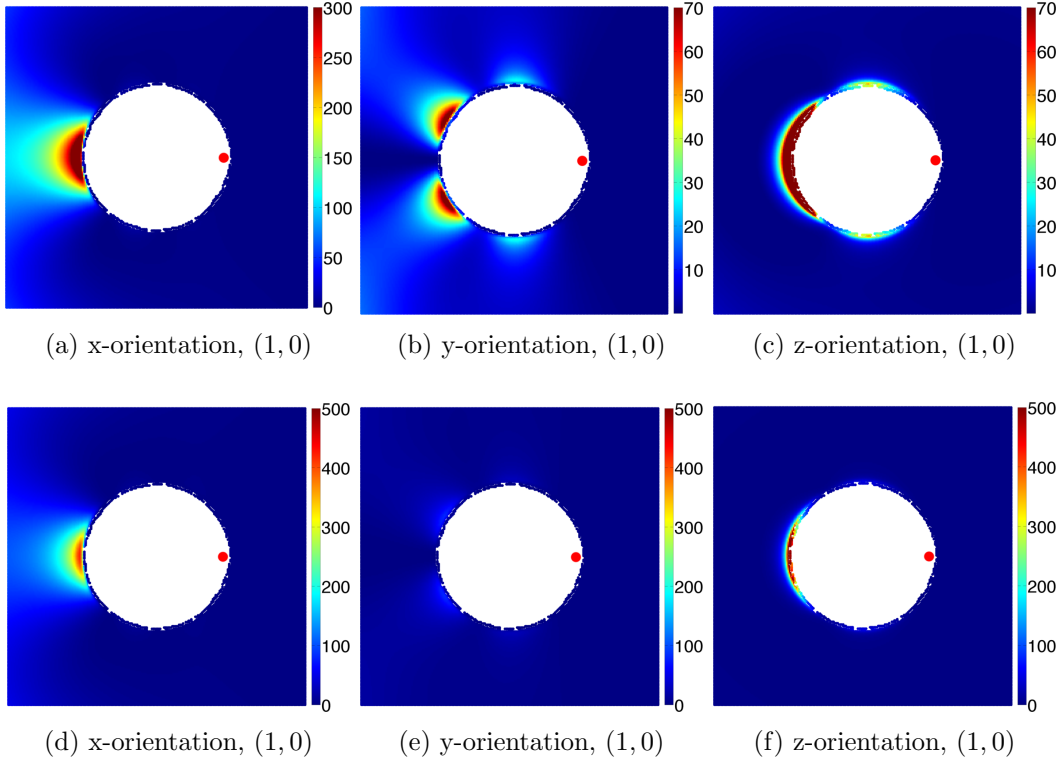


Fig. 4.23: $T(\omega)$ for a z-oriented molecule (red dot) emitting at the dipole's resonance frequency. The acceptors are placed outside of the disc (white space) and are aligned along the three axes (columns). Both rows show the same result but with different scales. The disc is 200 nm \times 30 nm, the index of the dielectric is 1.25. Donor and acceptors are 10 nm above the disc.

(Fig. 4.23c), energy is transferred to the poles of the mode. Again, it should be stated that $T(\omega)$ alone does not directly represent the energy transfer. If it wasn't for the strong dependence on the distance to the donor, the second pole would be visible on the right hand side of the disc. When the acceptors are oriented differently than the donor (Fig. 4.23a and Fig. 4.23b) the energy transfer is again most efficient at the poles but within them only in areas where the electric field of the mode that is excited (in this case the dipole mode) complies with the direction the acceptors are aligned in.

In the second row the scale is kept constant to be able to compare the strength depending on the acceptors' orientations. What we can learn from this is that the energy transfer is indeed stronger when the orientation of the donor is the same as the orientations of the acceptors.

The same is true for the quadrupole (Fig. 4.24). What's not visible in these plots is that the donor, being a dipole itself, splits up the pole it is situated close to. The rest of the circumference is then left for the remaining poles. In this case the donor

4 Results

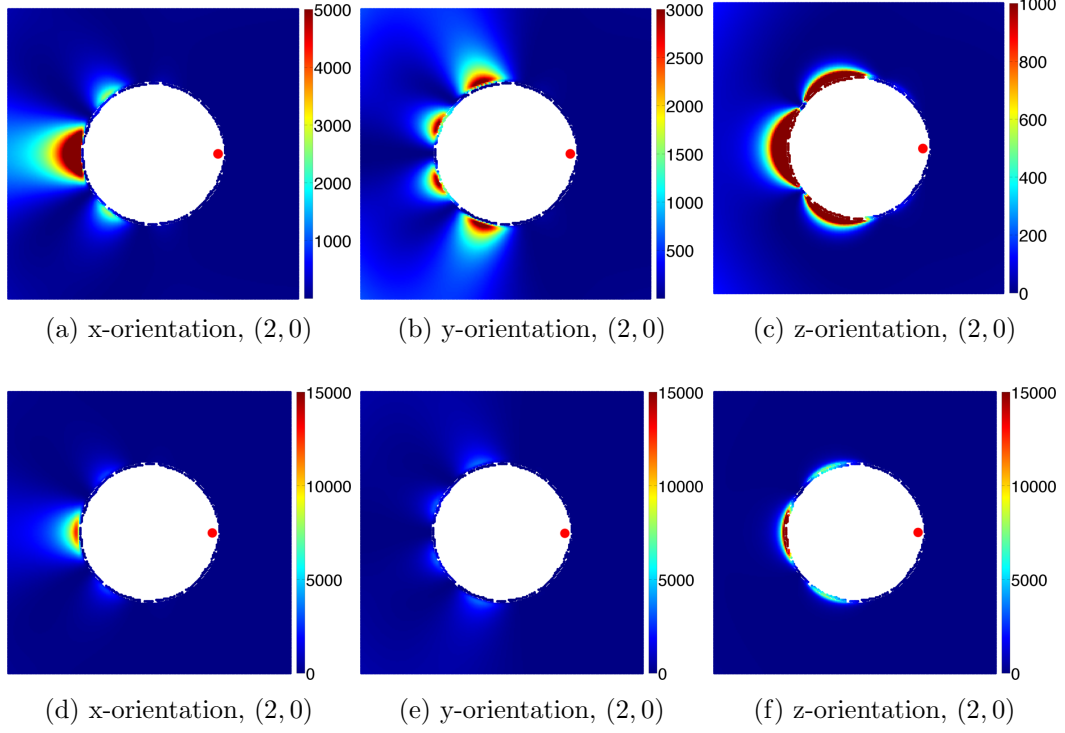


Fig. 4.24: Same setup as for Fig. 4.23, but with the donor set to the quadrupole's resonance frequency.

splits up the pole on the right hand side of the disc (which is hidden because of the R^6 dependence), and the rest of the space is divided by the three other poles.

The hexapole (Fig. 4.25) seems to be well suited for the purpose of actual energy transfer – note the scale, especially compared to the relatively damped dipole.

What we've stated above can maybe best be seen for the breathing mode's symmetry in Fig. 4.26. When both the donor and the acceptors point in the viewer's direction (4.26c), energy is transferred to the pole, which in this case is the whole circumference. When the acceptors are orientated along x (4.26a) or y (4.26b), those are activated that continue the radial line along which the breathing mode oscillates outwards.

The double breathing mode (Fig. 4.27) is also quite strong and influenced slightly by the very close bulk (shown in Fig. 4.28).

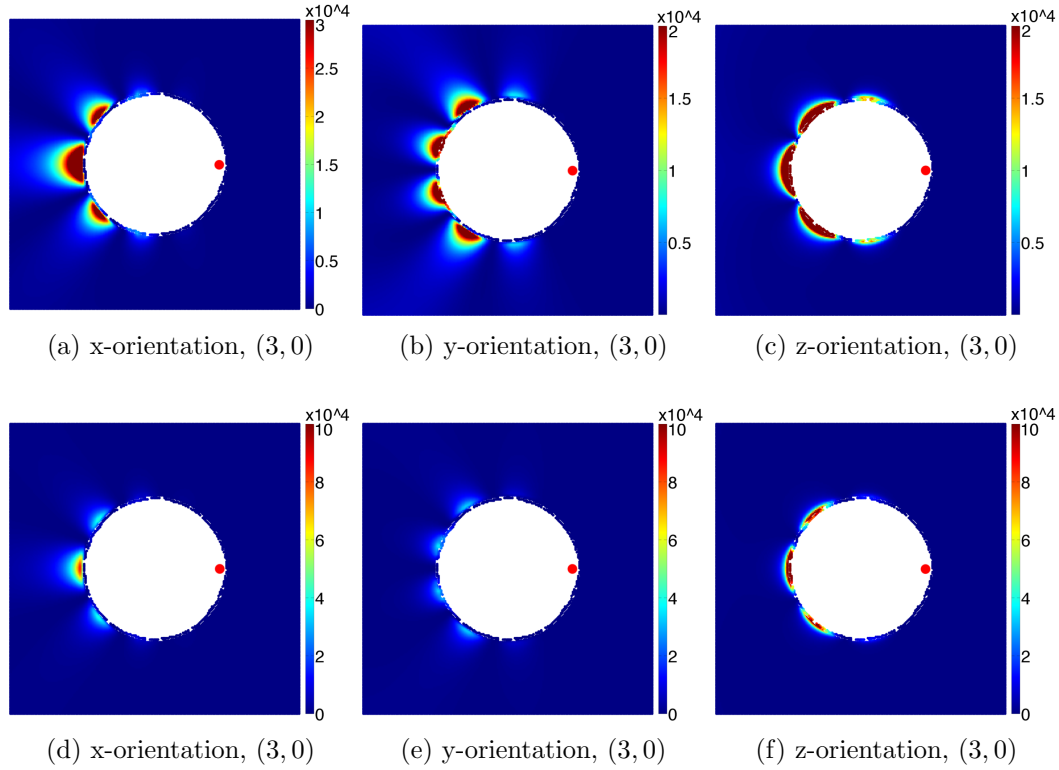


Fig. 4.25: Same setup as for Fig. 4.23, but with the donor set to the hexapole's resonance frequency.

4 Results

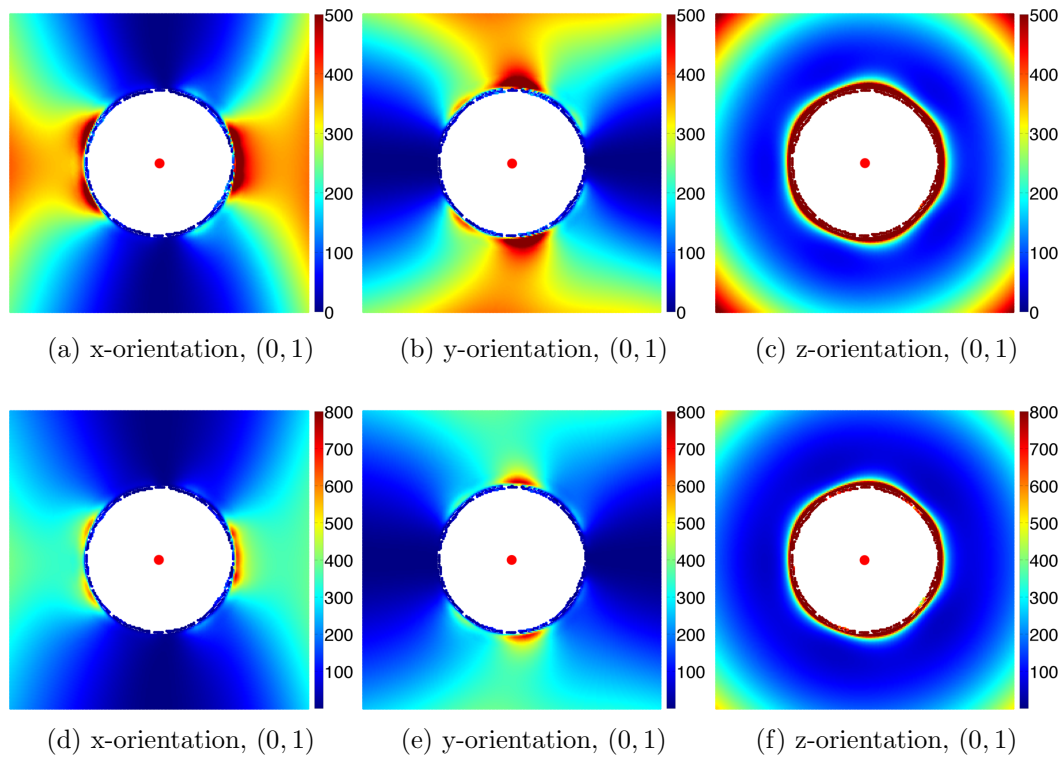


Fig. 4.26: Same setup as for Fig. 4.23, but with the donor set to the breathing mode's resonance frequency.

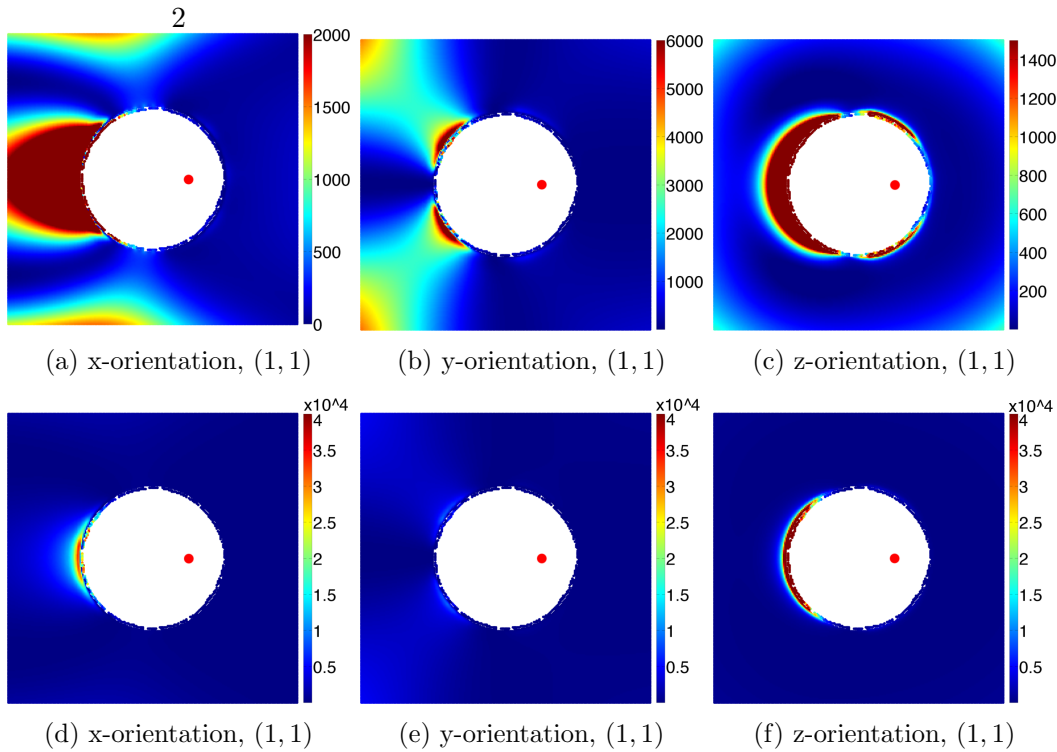


Fig. 4.27: Same setup as for Fig. 4.23, but with the donor set to the double breathing mode's resonance frequency.

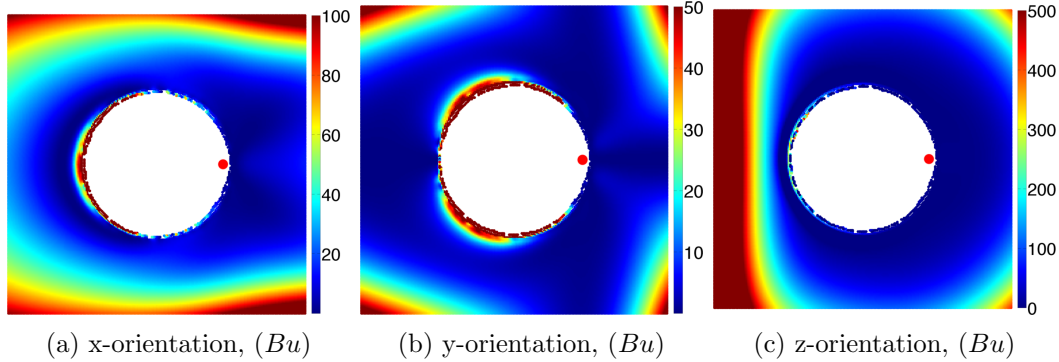


Fig. 4.28: Same setup as for Fig. 4.23, but with the donor set to the wavelength that excites the bulk.

5 Summary and outlook

5.1 Summary

This thesis shows that the classification dividing the mode spectrum of metallic nanoparticles into “bright” and “dark” plasmonic modes is somewhat arbitrary and interchangeable with the separation of dipole and non-dipole modes because none of them are truly optically dark for sufficiently (but not exceptionally) large nanodisks. Retardation effects and the breaking of the symmetry of an electromagnetic wave by using oblique light can be controlled to show the full mode spectrum of a nanodisk. The larger the disk is and the further the impinging light wave is tilted away from impact perpendicular to the disk’s surface the more higher order modes light up and radiate to the far field. If the angle is zero only the dipole mode and the double breathing mode as a hybrid of dipole and breathing mode show up. The spectrum is highly sensitive to the dielectric; a larger refractive index tends to make the peaks more distinguishable. Light needs to be p-polarized to be able to excite the breathing mode.

Although no direct comparison between optical excitation and the excitation by an electron beam is given, in both cases the individual modes are clearly identified by calculating their surface charge maps. The relative position and number of resonant wavelengths is the same for both approaches.

Analogous to the EELS simulation oscillating dipoles can also access the full mode spectrum. Edge and film modes are clearly separated; a dipole situated at the edge of the disk can excite the former, and one that is placed at the center can excite the latter. In between these positions the hybrid double breathing mode is visible. For a nanodisk in the xy-plane dipoles oriented along the z-axis can couple the strongest in all cases. In presence of the nanodisk, dipoles can use both the multipole and breathing modes to decay radiatively and is thus detectable in the far field. When a second dipole is included in the system, one of them can act as an energy donor and the other as an acceptor. The nanodisk helps to distribute this energy radiationlessly if it is tuned to have a resonant mode at the donor’s emission wavelength.

5.2 Outlook

Although theory and experiment were brought together very closely some discrepancies are not explained in this thesis, the most notable one being the absolute height of the peaks in scattering plots. We suspect that the reason for this is that the probes were fabricated on a glass substrate. We incorporated this in the simulations by

5 Summary and outlook

merely adjusting the refractive index of the dielectric but real *substrate effects* were not considered. The implementation of these effects in our simulation toolkit proves to be challenging and is currently being looked at by other group members. What would be easy to compute on the other hand is the direction of scattering, which we briefly looked at but neglected in the final form of this work. For some experimental setups with a limited field of view this might become more important.

Another point of concern are the *surface charges* we calculated throughout this thesis without giving a clear physical interpretation of what complex surface charges actually represent. We justify this by the visual clarity with which the modes can be seen by taking the real or imaginary part, and since the identification of modes is the only part of this thesis where we directly output the surface charges, this is certainly acceptable for our purpose. Still, an intuitive understanding remains elusive and will hopefully be the topic of a follow-up paper.

Regarding the mode spectrum we always included higher order multipole modes but focussed almost solemnly on the first order breathing mode – especially for the excitation with a plane wave. It might be interesting to take a computer with some free RAM, push retardation effects and stretch the spectrum with greater oblique angles, bigger discs, a large refractive index and a finer discretization of the discs' surfaces.

Finally, we admit that the quantum yield was calculated and presented in a number of plots but our interpretation remained very careful.

Certainly there are other aspects of the breathing modes worth investigating, and we are looking forward to new insights gained that may some day very well make the transition from basic research to common applications and find their way into technological devices.

6 Acknowledgements

My gratitude goes out to my teacher and supervisor of this thesis Ao. Univ. Prof. Dr. ULRICH HOHENESTER. He shares some of my interests outside of Physics and without compromising the quality of work not once raised my stress level. Not to mention that his understanding of Physics is inspirational. Together with his colleague and my friend Mag. Dr.rer.nat. ANDREAS TRÜGLER he developed the working horse for plasmonic research in our group – the MNPBEM toolbox without which my thesis would have looked differently in one way or another.

I want to thank Univ. Prof. Mag. Dr.rer.nat. JOACHIM KRENN and his strong experimental nano optics group for the infrastructure they provided and Dipl.-Ing. BSc MARKUS KRUG in particular who took it upon himself to dedicate his thesis to investigating the findings experimentally. It is always nice to have theory and experiment come together, as well as receiving input from a different perspective.

Although I'll only mention the group members Mag.rer.nat. JAKOB EBNER and Bakk.rer.nat. MSc ANTON HÖRL all my early and late friends should feel included for accompanying me on my way.

And, most importantly, none of this would have been possible without the lovely connection with my parents and their unlimited support in every aspect of my life. Thank you.

Bibliography

- [AHL⁺08] J. N. Anker, W. P. Hall, O. Lyandres, N. C. Shah, J. Zhao, and R. P. Van Duyne. Biosensing with plasmonic nanosensors. *Nature Materials*, 7:442–453, 2008.
- [Atw07] H. A. Atwater. The promise of plasmonics. *Scientific American*, 56, 2007.
- [AvEW02] E. Altewischer, M. P. van Exter, and J. P. Woerdman. Plasmon-assisted transmission of entangled photons. *Nature*, 418, 2002.
- [BH83] C. F. Bohren and D. R. Huffman. *Absorption and Scattering of Light by Small Particles*. Wiley and Sons, Inc., 1983.
- [BTJ⁺10] J. Becker, A. Trügler, A. Jakab, U. Hohenester, and C. Sönnichsen. The optimal aspect ratio of gold nanorods for plasmonic bio-sensing. *Plasmonics* 5, 161, 2010.
- [dA02] F. J. García de Abajo. Retarded field calculation of electron energy loss in inhomogeneous dielectrics. *Phys. Rev. B*, 65(115418), 2002.
- [Dem06] W. Demtröder. *Experimentalphysik 2 - Elektrizität und Optik*. Springer, 4th edition, 2006.
- [DF94] B. T. Draime and Piotr J. Flatau. Discrete-dipole approximaton for scattering calculations. *J. Opt. Soc. Am. A*, 11(4), 1994.
- [ESHES05] I. H. El-Sayed, X. Huang, and M. A. El-Sayed. Selective laser photo-thermal therapy of epithelial carcinoma using anti-EGFR antibody conjugated gold nanoparticles. *Cancer Lett.*, 239:129–135, 2005.
- [Fer32] E. Fermi. Quantum theory of radiation. *Reviews of modern Physics*, 1932.
- [Gre28] G. Green. An essay on the application of mathematical analysis to the theories of electricity and magnetism. *orig. publ. Nottingham*, 1828.
- [GRH⁺07] S. Gerber, F. Reil, U. Hohenester, T. Schlagenhaufen, J. Krenn, and A. Leitner. Tailoring light emission properties of fluorophores by coupling to resonance-tuned metallic nanostructures. *Phys. Rev. B*, 75, 2007.

Bibliography

- [HK05] U. Hohenester and J. Krenn. Surface plasmon resonances of single and coupled metallic nanoparticles: A boundary integral method approach. *Phys. Rev. B*, 2005.
- [HLA⁺08] F. Hao, E. M. Larsson, T. A. Ali, D. S. Sutherland, and P. Nordlander. Shedding light on dark plasmons in gold nanorings. *Chem. Phys. Lett.*, 458:262–266, 2008.
- [Hoh14] U. Hohenester. Simulating electron energy loss spectroscopy with the MNPBEM toolbox. *Comp. Phys. Commun.*, 185(1177), 2014.
- [HT08] U. Hohenester and A. Trügler. Interaction of single molecules with metallic nanoparticles. *IEEE Journal of Selected Topics in Quantum Electronics*, 14, 2008.
- [HT11] U. Hohenester and A. Trügler. MNPBEM - a Matlab toolbox for the simulation of plasmonic nanoparticles. *Comp. Phys. Commun.*, 183, 2011.
- [Jac98] J. D. Jackson. *Classical Electrodynamics*. Wiley and Sons, Inc., 3rd edition, 1998.
- [JC72] P. B. Johnson and R. W. Christy. Optical constants of the noble metals. *Phys. Rev. By*, 6, 1972.
- [Kru14] Markus Krug. *Bright and Dark Plasmonic Modes of Silver Nanodisks*. PhD thesis, Graz University of Technology, 2014.
- [LHPAD04] F. Ladstädter, U. Hohenester, P. Putschnig, and C. Ambrosch-Draxl. First-principles calculation of hot-electron scattering in metals. *Phys. Rev. B*, 70, 2004.
- [Lor67] L. Lorenz. On the identity of the vibrations of light with electrical currents. *Phil. Mag.*, 34, 1867.
- [Mai07] S. A. Maier. *Plasmonics: Fundamentals and applications*. Springer, 1st edition, 2007.
- [Max65] J. C. Maxwell. A dynamical theory of the electromagnetic field. *Phil. Trans. R. Soc. Lond.*, 155:459–512, 1865.
- [Mie08] G. Mie. Beiträge zur Optik trüber Medien, speziell kolloidaler Metallösungen. *Annalen der Physik*, pages 330–445, 1908.
- [NH06] L. Novotny and B. Hecht. *Principles of Nano-Optics*. Cambridge University Pres, 2006.
- [Pal85] E. D. Palik. *Handbook of Optical Constants of Solids*. Academic Press, New York, 1985.

Bibliography

- [PJPSLMM05] J. Pérez-Juste, I. Pastoriza-Santos, L. M. Liz-Marzán, and P. Mulvaney. Gold nanorods: Synthesis, characterization and applications. *Coord. Chem. Rev.*, 249:1870–1901, 2005.
- [SDH⁺12] F-P. Schmidt, H. Ditlbacher, U. Hohenester, A. Hohenau, F. Hofer, and J. Krenn. Dark plasmonic breathing modes in silver nanodisks. *Nano Letters*, 12, 2012.
- [Trü11] A. Trögler. *Optical properties of metallic nanoparticles*. PhD thesis, Institut für Theoretische Physik, Karl-Franzens-Universität Graz, 2011.
- [vdH81] H. C. van de Hulst. *Light scattering by small particles*. Dover Publications Inc., 1981.
- [ZCG09] P. Zijlstra, J. W. M. Chon, and M. Gu. Five-dimensional optical recording mediated by surface plasmons in gold nanorods. *Nature*, 459, 2009.
- [ZPN09] J. Zuloaga, E. Prodan, and P. Nordlander. Quantum description of the plasmon resonances of a nanoparticle dimer. *Nano Letters*, 9(2):887–891, 2009.

List of Figures

1.1	The Lycurgus cup	1
2.1	Field lines of an electric dipole	6
2.2	Sketch of the Boundary Element Method	10
2.3	Dielectric function of gold for experiment and theory	13
2.4	Dielectric function of gold and silver	14
2.5	Rayleigh scattering by a dipole	17
2.6	Setup for the energy transfer between donor and acceptor molecules . .	20
2.7	The function $T(\omega)$ scaling energy transfer between dipoles	22
2.8	Particle plasmon	25
2.9	Dispersion relation for a surface plasmon	26
2.10	Otto and Kretschmann configurations to excite surface plasmons . . .	27
2.11	Multipole and breathing modes with node lines	28
3.1	Retardation via oblique light	32
3.2	Experimental spectra for tuned nanodiscs	33
3.3	Possible simulations within the MNPBEM toolbox	37
3.4	Building a nanodisc within the MNPBEM-toolbox	37
3.5	Flow chart for MNPBEM-simulations	38
4.1	Setup for EELS simulation	39
4.2	EELS map for a silver nanodisc	40
4.3	Surface charges of the breathing mode	41
4.4	Surface charges of multipole and breathing modes	42
4.5	Attempts to excite modes at the wrong spatial position	43
4.6	Scattering cross section for plane wave excitation (straight impact) .	44
4.7	Scattering cross section for plane wave excitation (tilted impact) .	45
4.8	Scattering cross section for different angles of oblique light	46
4.9	Scattering cross section dependent on the disc size for plane wave excitation	47
4.10	Dependence on the polarization of the scattering cross section for plane wave excitation	48
4.11	Dependence on the refractive index of the scattering cross section for plane wave excitation	49
4.12	Comparison of the scattering cross sections of silver and gold	50
4.13	Decay rate of a dipole on the edge of a nanodisc	51
4.14	Decay rate of a dipole at the center of a nanodisc	52

List of Figures

4.15 Decay rate of a dipole situated between the center and the edge of a nanodisc	53
4.16 Radiative decay rates for different dipole positions and energies	53
4.17 Decay rate of dipoles depending on their orientation to the nanoparticle	54
4.18 Setup for measuring the quantum yield	55
4.19 Quantum yield for dipoles with different positions and energies	55
4.20 Quantum yield for selected modes	56
4.21 Comparison of the quantum yield for different dipole orientations	57
4.22 $T(\omega)$ scaling the energy transfer for a donor in free space	58
4.23 $T(\omega)$ at the resonance for the dipole mode	59
4.24 $T(\omega)$ at the resonance for the quadrupole mode	60
4.25 $T(\omega)$ at the resonance for the hexapole mode	61
4.26 $T(\omega)$ at the resonance for the breathing mode	62
4.27 $T(\omega)$ at the resonance for the double breathing mode	63
4.28 $T(\omega)$ at the resonance for the bulk	63